JGR Solid Earth

RESEARCH ARTICLE
10.1029/2021JB022155

Improving Absolute Hypocenter Accuracy With 3D *Pg* and *Sg* Body-Wave Inversion Procedures and Application to Earthquakes in the Central Alps Region

Tobias Diehl[1], Edi Kissling[2], Marco Herwegh[3], and Stefan M. Schmid[2]

[1]Swiss Seismological Service, ETH Zurich, Zurich, Switzerland, [2]Institute of Geophysics, ETH Zurich, Zurich, Switzerland, [3]Institute of Geological Sciences, University of Bern, Bern, Switzerland

Key Points:

- Sub-kilometer hypocenter accuracy is achieved with dynamically selected *Pg* and *Sg* phases, in combination with 3D crustal velocity models
- New 3D V_P and V_S models image the upper crust of the Central Alps region at unprecedented resolution
- Joint interpretation of relocated hypocenters and seismic velocities can constrain lithologies hosting seismicity in the Central Alps

Supporting Information:

Supporting Information may be found in the online version of this article.

Correspondence to:

T. Diehl,
tobias.diehl@sed.ethz.ch

Citation:

Diehl, T., Kissling, E., Herwegh, M., & Schmid, S. M. (2021). Improving absolute hypocenter accuracy with 3D Pg and Sg body-wave inversion procedures and application to earthquakes in the Central Alps region. *Journal of Geophysical Research: Solid Earth*, *126*, e2021JB022155. https://doi.org/10.1029/2021JB022155

Received 31 MAR 2021
Accepted 5 NOV 2021

Author Contributions:

Conceptualization: Tobias Diehl, Edi Kissling, Marco Herwegh, Stefan M. Schmid
Formal analysis: Tobias Diehl
Investigation: Tobias Diehl, Edi Kissling, Marco Herwegh, Stefan M. Schmid
Methodology: Tobias Diehl, Edi Kissling
Software: Tobias Diehl, Edi Kissling
Visualization: Tobias Diehl, Marco Herwegh, Stefan M. Schmid
Writing – original draft: Tobias Diehl

Abstract Accuracy of hypocenter location, in particular focal depth, is a precondition for high-resolution seismotectonic analysis of natural and induced seismicity. For instance, linking seismicity with mapped fault segments requires hypocenter accuracy at the sub-kilometer scale. In this study, we demonstrate that inaccurate velocity models and improper phase selection can bias absolute hypocenter locations and location uncertainties, resulting in errors larger than the targeted accuracy. To avoid such bias in densely instrumented seismic networks, we propose a coupled hypocenter-velocity inversion procedure restricted to direct, first-arriving, mainly upper-crustal *Pg* and *Sg* phases. On the basis of synthetic tests and selected ground-truth events we demonstrate that a sub-kilometer hypocenter accuracy can be achieved by regional-scale, three-dimensional *Pg* and *Sg* velocity models combined with dynamic phase selection and a non-linear location algorithm. The tomographic inversion uses about 60,000 *Pg* and 30,000 *Sg* quality-checked phases of local earthquakes in the Central Alps region. The derived models image the V_P and V_S structure of the Central Alps upper crust at unprecedented resolution, including small-scale anomalies such as those caused by Subalpine Molasse units below the Alpine front. The relocation procedure is applied to more than 18,000 earthquakes and the relocated hypocenters reveal previously unrecognized seismogenic structures, for instance in the Swiss Molasse basin south of Bern. The M_L 4.6 Urnerboden earthquake of 2017 is used as an example to demonstrate how the derived 3D velocity structure and relocated hypocenters can be jointly interpreted to constrain the lithology hosting upper-crustal seismicity in the Central Alps.

Plain Language Summary To better understand how mountain belts like the European Alps presently deform and what are the plate-tectonic forces driving this deformation requires accurate knowledge of the location of earthquakes within these continental collision zones. In this study, we achieve an accuracy of less than a kilometer for earthquake locations in Switzerland, based on detailed knowledge of the subsurface structure of the Earth's crust. We use three-dimensional tomographic imaging methods to improve subsurface structural models of the Central Alps. These models also provide new insights into the geological structure of this mountain range and in combination with the improved earthquake locations allow for detailed studies of present-day tectonic processes.

1. Introduction

The accuracy of absolute hypocenter location of natural and induced seismicity is a crucial parameter to understand seismotectonic processes at high resolution. Mainly due to poor hypocenter depth resolution, a recurrent problem in seismotectonic interpretation of upper-crustal seismicity relates to the question whether earthquakes are located on faults only affecting the sedimentary cover, restricted to the crystalline basement or along faults cutting across the sediment-basement contact. The exact knowledge of the lithology that hosts a seismogenic fault is crucial, for instance, for earthquake-triggering models. It is therefore especially important to understand the mechanisms of induced seismicity and its connection to hydraulic conditions in the uppermost crust (e.g., Ellsworth, 2013). Furthermore, the discrimination between sources hosted in sediments from those in the crystalline basement allows conclusions on the style of tectonic deformation in orogenic belts and related foreland basins, in particular, to answer the question if present-day strain is coupled across first-order lithological boundaries, for example, the basement-cover contact, or not (e.g., Mock & Herwegh, 2017; Mosar, 1999; Pfiffner, 2017; Ustaszewski & Schmid, 2007).

Writing – review & editing: Edi Kissling, Marco Herwegh, Stefan M. Schmid

Unless direct information, for example, from refracted, reflected, or converted seismic phases is available (e.g., Goertz-Allmann et al., 2017; Kim et al., 2006; Ma, 2010), such discrimination requires focal-depth accuracy at the sub-kilometer scale or smaller, and additionally, accurate structural models of the basement topography. As demonstrated, for example, by Diehl et al. (2017), additional constraints on the lithology might be deduced from seismic velocities in the source region determined by tomographic methods.

Furthermore, seismicity might be associated with geologically or geophysically mapped fault segments (line sources) or distributed in an area (area sources). A direct link between line sources and mapped faults is of major importance for high-resolution seismotectonic interpretation and seismic hazard assessment. It allows, for instance, the study of rupture processes and interaction of faults. This link is therefore also key to improve the management of fluid injections in geo-energy applications, aiming to minimize the risk of triggering felt earthquakes (e.g., Diehl et al., 2017; Gaucher et al., 2015). In order to assign earthquakes to individual segments of a fault system, however, requires hypocenter accuracy at the scale of kilometers or smaller.

A better understanding of ongoing brittle deformation in continental collision zones like the Central Alps region (Figure 1) therefore requires procedures to achieve the targeted sub-kilometer hypocenter accuracy, together with high-resolution seismic velocity models constraining lithological units within the upper crust. In this study, we first quantify the effects of improper velocity models and seismic phase selection on hypocenter accuracy and precision by a series of synthetic tests. In order to achieve the targeted sub-kilometer location accuracy, we propose a coupled velocity-hypocenter inversion restricted to direct, mainly upper-crustal *Pg* and *Sg* phases. This procedure is based on the independent inversion of *P* and *S* data, which allows for a consistent quality control of the arrival-time data as well as for an unbiased computation of crustal *P* and *S* wave velocities. We apply this strategy to high-quality arrival-time data from the densely instrumented region of the Central Alps and their foreland (Figure 1a) and derive high-resolution, three-dimensional (3D) *P* and *S* wave velocity models of the uppermost crust. The new V_P and V_S models, combined with a dynamic phase-selection procedure and a nonlinear hypocenter location algorithm, are used to consistently relocate the entire instrumental earthquake bulletin of the Swiss Seismological Service (SED) in the period of 1984–2020. We assess accuracy and precision of the relocated catalog by comparison with selected ground-truth (GT) events. Using the example of the M_L 4.6 Urnerboden earthquake of 2017, we finally demonstrate how joint interpretation of velocity models and relocated seismicity provides constraints on lithologies hosting upper-crustal seismicity in the Central Alps region.

2. Methods to Improve Hypocenter Accuracy in the Central Alps

2.1. Hypocenter Accuracy and Its Dependency on Velocity Models and Phase Selection

Uncertainties in hypocenter location are commonly quantified by two terms: precision and accuracy (e.g., Husen & Hardebeck, 2010). Hypocenter precision describes the error in relative position of nearby hypocenters. This scatter is caused, for instance, by noise in the measurements of arrival times. An estimate of the precision of a single hypocenter is therefore provided by the formal location error, which considers network geometry (primarily azimuthal gap and distance to closest observing station), observation errors (uncertainties of arrival-time picks), and phase types (e.g., usage of depth phases or other reflected phases) (e.g., Bondár et al., 2004; Engdahl et al., 1998; Gomberg et al., 1990; Husen & Hardebeck, 2010). Hypocenter precision on its own, however, does not quantify absolute hypocenter accuracy and does not always represent the true error, since it neglects the errors in the used velocity model (e.g., Pavlis, 1986). Different attempts were made to consider the velocity-model errors in the formal location error (e.g., Lomax et al., 2000; Moser et al., 1992; Pavlis, 1986), for instance, by approximating the velocity-model errors by Gaussian travel-time errors. The *Nonlinloc* (NLL) location algorithm (Lomax et al., 2000, 2014) used in in this study, combines hypocenter precision with first-order accuracy estimates in the formal location errors. Therefore, these errors represent a more realistic hypocenter uncertainty (see Supporting Information S1 provided in the electronic supplement for details on the location uncertainties of NLL). The assumption of Gaussian travel-time errors can, however, underestimate the true uncertainties because it neglects systematic errors in the used velocity model and phase misidentifications in the arrival-time data (e.g., Husen & Hardebeck, 2010). To achieve the targeted sub-kilometer hypocenter accuracy and to benefit from additional constraints provided by secondary arrivals, velocity models need to be highly accurate for all *P* and *S* waves used in the location process, including direct, refracted, and possible reflected phases. Common 1D and 3D hypocenter-velocity inversion methods to derive such models at local to regional scales, as well as shortcomings

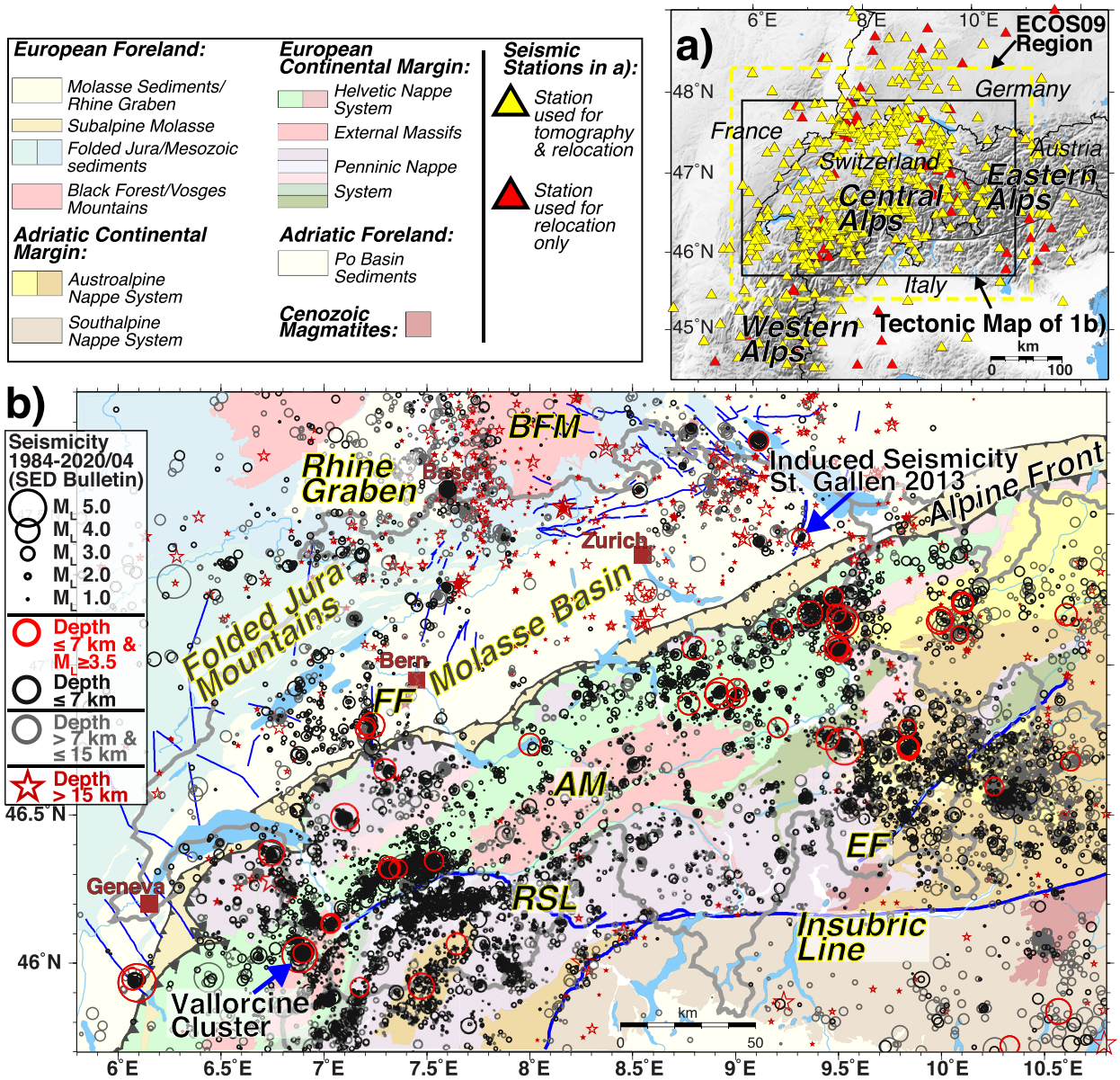

Figure 1. Map summarizing geology, seismicity, and seismic stations in the Central Alps region. (a) Overview map showing the central part of the Alpine Arc with seismic stations used in this study. (b) Major tectonic units, Alpine front (gray lines), and fault systems (blue lines) in the Central Alps and their northern foreland (after Heuberger et al., 2016; Mock & Herwegh, 2017; Pfiffner, 2014; Swisstopo, 2005; Vouillamoz et al., 2017). Circles mark instrumentally located earthquakes in the uppermost crust (focal depth ≤15 km) as reported in the earthquake bulletin of the SED between 1984 and April 2020. Black circles correspond to shallow seismicity (focal depth ≤ 7 km) and red circles indicate shallow earthquakes (focal depth ≤ 7 km) with local magnitudes $M_L \geq 3.5$. Red asterisks mark earthquakes in the lower part of the crust (focal depth >15 km). AM, Aar Massif; BFM, Black-Forest Massif; EF, Engadine Fault; FF, Fribourg Fault Zone; RSL, Rhone-Simplon Line.

associated with them, are summarized in detail in Supporting Information S1 provided in the electronic supplement. The inversion strategy used in this study is described in Section 2.2.

In addition, the distance range selected for hypocenter inversion can have a significant impact on the location accuracy. Figure 2 sketches the main crustal phases (direct and refracted rays) commonly used for hypocenter location at local to regional distances and shows the corresponding travel times for a simplified two-layer crustal model. The focal depth is mainly constrained by direct phases, observed within epicentral distances of about 1–1.5 times the focal depth (e.g., Chatelain et al., 1980; Gomberg et al., 1990). If such close-by observations are lacking, critically Moho-refracted *Pn* (Figure 2) or Moho-reflected *PmP* phases can be used to constrain focal-depth estimates, since these phases extend the range of take-off angles (e.g., Ma, 2010; Stroujkova, 2009;

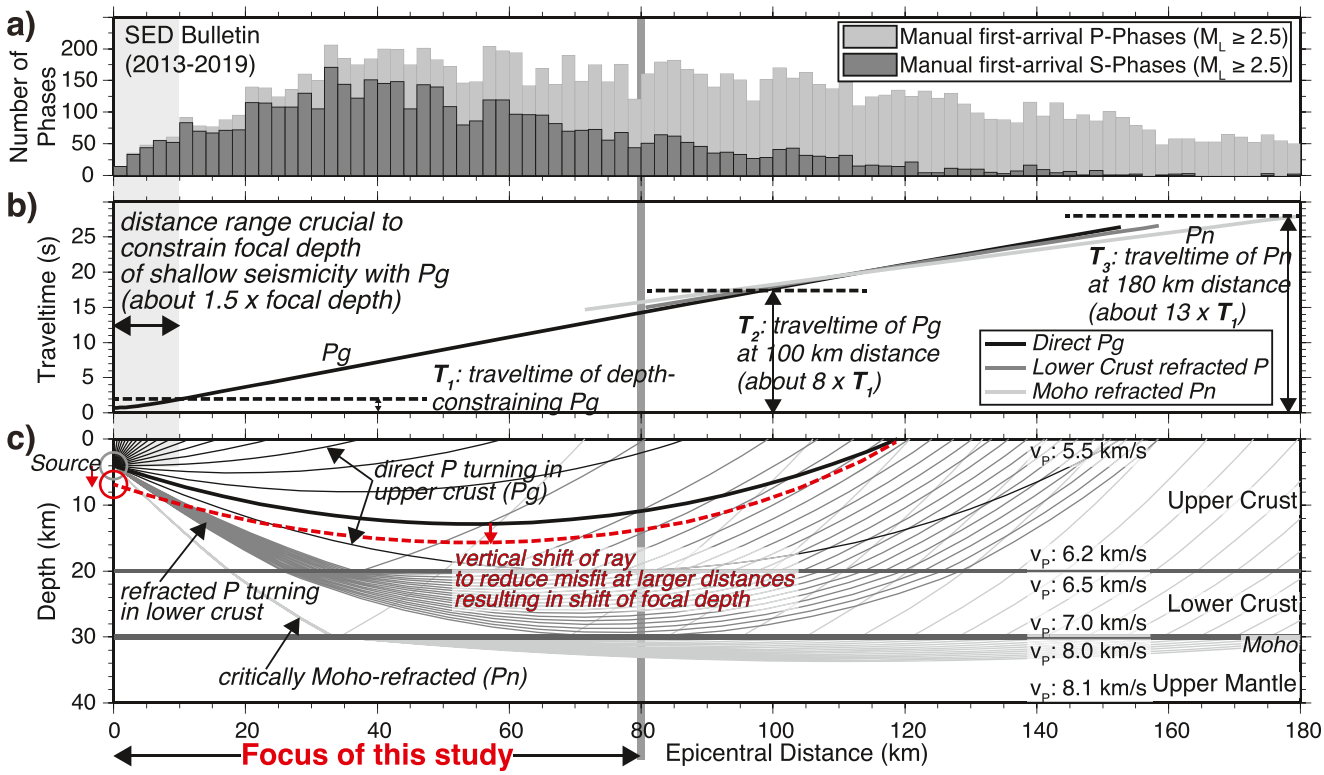

Figure 2. Data distribution, travel times, and ray geometries of direct and refracted crustal phases typically used for earthquake location and tomography at local to regional distances. (a) Epicentral distribution of *P* and *S* wave arrival times reported in the bulletin of the SED for earthquakes of $M_L \geq 2.5$ in the period 2013–2019. (b) Travel time as a function of epicentral distance calculated with the *MacRay* software (Luetgert, 1992) for a simplified crustal model shown in (c). (c) Ray geometries of direct *Pg*, refracted and critically Moho refracted (*Pn*) phases. Geometry and travel times of long-distance rays are strongly affected by the velocity structure and potential modeling errors accumulated along these rays can result in significant focal-depth errors.

Wagner et al., 2013). As documented by Figure 2, the use of observations at larger distances may, however, be problematic for two reasons: (a) above certain magnitudes (in the example of Switzerland, e.g., $M_L \geq 2.5$), observations at larger distances can outnumber the observations near the epicenter (Figure 2a) and therefore reduce the relative weight of the depth-constraining *Pg* and *Sg* phases in the hypocenter inversion. (b) Raypath geometry as well as travel times of long-distance rays are more strongly affected by the 3D velocity structure compared to short-distance (e.g., upward-going) direct rays (Figures 2b and 2c). Long-distance rays therefore accumulate more potential modeling errors resulting in larger travel-time residuals. If systematic, such residuals are compensated by vertical shifts of the corresponding ray paths in the hypocenter inversion, leading to errors in focal depth (Figure 2c).

We performed a series of synthetic tests to quantify the effect of the 3D velocity structure on hypocenter accuracy and precision, and their dependency on the phases (ray paths) selected for hypocenter inversion. For this test we calculated synthetic *P* and *S* wave arrival times in 3D crustal *P* and *S* wave velocity models. These 3D models represent earlier versions of the tomographic models of the Central Alps presented later in this study. Synthetic travel times were calculated for a real receiver geometry of an M_L 3.3 earthquake analyzed by the SED, which occurred close to Vallorcine (Figure 1b), in the border region between France and Switzerland on March 20, 2017. The closest station is located at an epicentral distance of about 4 km (minimum distance: *mdi*). The focal depth was set to 4 km for the synthetic test and quality-class dependent Gaussian errors (average absolute errors: 0.13 s; minimum error: −0.7 s; maximum error: +0.6 s) were added to the synthetic travel times, mimicking the manual pick qualities of this event. Synthetic travel times were inverted for hypocentral parameters using the NLL location algorithm with an *L*2-misfit function. For hypocenter inversion, we applied 1D *P* and *S* wave velocity models, which are earlier versions of the 1D models presented later in this study and represent the 1D reference of the 3D models used to calculate the synthetic travel times. Hypocenter inversions were performed with arrival-time picks from a range of epicentral distances by increasing the maximum epicentral distance in steps of 10 km between

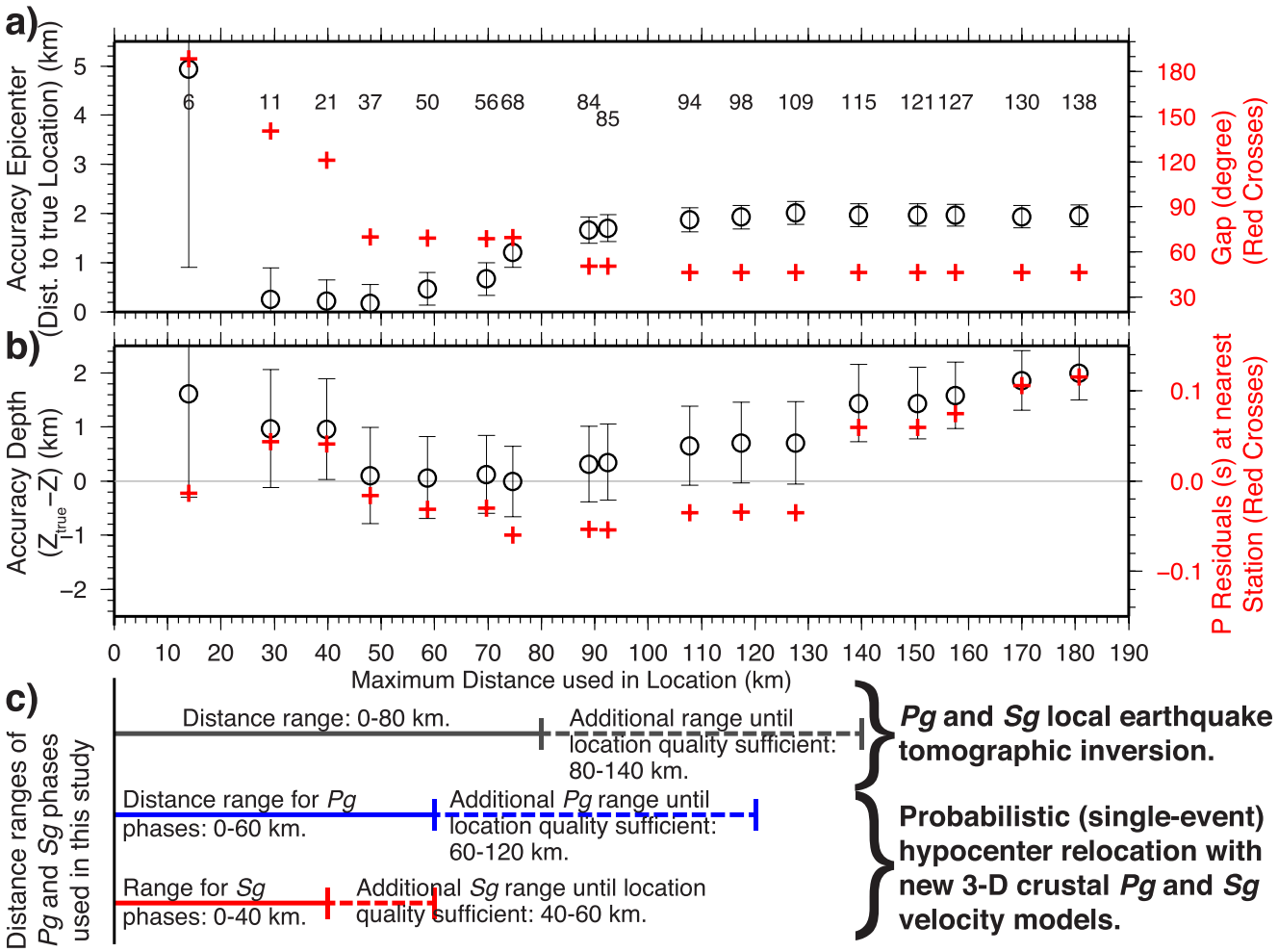

Figure 3. Synthetic test quantifying the effect of 3D velocity structures and the dependency of hypocenter precision and accuracy on the distance range of phases used in the hypocenter inversion. Synthetic travel times are calculated in 3D crustal *P* and *S* wave velocity models. The hypocenter inversion was performed with 1D *P* and *S* wave models. (a) Error (accuracy) between true epicenter and hypocenter inversion using different maximum epicentral distances. Numbers indicate the number of observations available for the corresponding distance range. Error bars correspond to the maximum horizontal 1σ location uncertainty of the *Nonlinloc* (NLL) algorithm, which represents a ("pessimistic") estimate of the precision. Red crosses indicate the azimuthal gap of the corresponding solution. (b) Error (accuracy) between true focal depth and hypocenter inversion as described for (a). Error bars correspond to 1σ NLL depth uncertainties ("pessimistic" precision estimate). Red crosses indicate the travel-time residual of the station closest to the epicenter (in about 4 km distance). (c) Summary of distance ranges used for tomography and relocation methods in this study.

20 and 190 km. Figure 3 shows the resulting precision and accuracy as a function of the maximum epicentral distance for epicenter and focal depth. It should be noted that here (and in the following sections), hypocenter precision corresponds to the 1σ location errors computed by NLL (for details see Supporting Information S1). As described above, this error includes a first-order estimate of the velocity-model error and is therefore larger than standard precision estimates that neglect model errors.

Using *P* and *S* phases between 0 and 20 km distance for hypocenter inversion results in relatively large epicentral (precision: ±4.0 km; accuracy: 4.9 km) and focal-depth uncertainties (precision: ±1.9 km; accuracy: 1.6 km; Figure 3). This is due to the low number of observations (*nobs*) of 6 and an azimuthal gap (*gap*) >180°. Using phases between 0 and 30 km reduces the *gap* (<180°), which results in a sub-kilometer epicentral accuracy (0.3 km) and a realistic epicenter precision of ±0.7 km (including the true epicenter). The focal-depth accuracy is on the order of 1 km with a precision of ±1 km (including the true depth). The highest focal-depth accuracy is achieved using phases up to 50–80 km distance, resulting in accuracies in the sub-kilometer scale (<0.2 km) and precision on the order of ±1 km (Figure 3b). On the other hand, epicenter accuracy worsens for distances >50 km (accuracy >1 km), and corresponding epicenter precision becomes unrealistically small (about 0.3 km; Figure 3a). From

additional tests using an idealized, synthetic receiver geometry, we conclude that the increasing error in epicenter locations for distances >50 km is related to 3D velocity structures not included in the 1D models used in the hypocenter inversion.

Finally, using phases at distances >80 km results in a gradual loss of focal-depth accuracy (systematic errors in focal depth up to 2 km), whereas focal-depth precision decreases to unrealistically small values (Figure 3b). For distances >140 km, precision becomes smaller than accuracy (i.e., not including the true depth anymore) and, at the same time, the travel-time residual at the closest station gradually increases. This increase indicates that the solution is dominated by fitting long-distance phases, but is inconsistent with actual depth-constraining observations close to the source.

From this synthetic test, we conclude that a sub-kilometer accuracy of epicenter and focal depth can be achieved using direct, first-arriving *Pg* and *Sg* phases up to about 80 km epicentral distance. These direct *Pg* and *Sg* phases have ray geometries similar to those shown in Figure 2c, with turning points mainly located within the upper crust. This strategy requires a dense network of seismometers to ensure depth-constraining *P* and *S* observations at distances within about 1.5 times the focal depth. A uniform station spacing on the order of 20 km would therefore yield a vertical constraint for true focal depths ≥6 km. In addition, the tests in Figure 3 confirm that an accurate velocity model of the upper crust is required to account for 3D effects and to avoid systematic errors as documented for epicenters for distances >50 km in Figure 3a.

2.2. Inversion Strategy to Derive V_P and V_S Models for Accurate Hypocenter Location

To achieve the required velocity-model accuracy and to avoid any bias mapped into the tomographic models by the focal-depth errors documented in Figure 3b, we propose a coupled hypocenter-velocity inversion restricted to direct, mainly upper-crustal first-arriving *Pg* and *Sg* phases with ray paths illustrated in Figure 2c. In the presence of a dense seismic network and well-distributed seismicity, as is the case in the Central Alps region (Figure 1), tomographic resolution is expected to be excellent within the upper 10–20 km of the crust. In addition, quality of travel-time data is expected to be highest for direct *Pg* and *Sg* arrivals, since onsets within the targeted distance range are usually clear and impulsive and less contaminated by misidentifications of phases (e.g., Diehl, Kissling, Husen, & Aldersons, 2009).

As shown by Gomberg et al. (1990), the use of *S* phases provides a powerful constraint on focal-depth estimates. However, the simultaneous use of *P* and *S* phases for hypocenter determination requires accurate and compatible V_P and V_S models in order to avoid any bias in the resulting hypocenter solutions. For instance, Maurer and Kradolfer (1996) demonstrate that neglecting variations in the V_P/V_S ratio may result in hypocenter solutions that are less accurate than those using *P* wave data alone. Different strategies have been proposed to derive such compatible V_P and V_S models. A common approach is the joint inversion of *P* and *S* data to derive 1D or 3D $V_P + V_P/V_S$ models (e.g., Eberhart-Phillips, 1990; Thurber, 1993) or $V_P + V_S$ (e.g., Husen et al., 1999; Maurer & Kradolfer, 1996; Tryggvason et al., 2002). The joint inversion assumes the same hypocenter for the corresponding *P* and *S* waves and can theoretically stabilize the inversion of V_P/V_S or V_S models. Therefore, these methods were originally developed for cases for which the quantity or quality of *S* data were insufficient for an independent inversion. In the upper crust, V_P and V_S depend mainly on petrophysical properties of the different lithologies and are, therefore, by no means linearly related. The joint approach, however, requires a priori assumptions on the relation between V_P and V_S. In the linearized inversion, this relation is controlled by the data weighting, damping values (for hypocentral and velocity parameters), maximum adjustments of parameters per iteration and initial values (hypocenters and velocities). Considering the common imbalance between *P* and *S* data (*P* observations outnumber *S* in quantity and quality), the choice of these parameters becomes problematic. Especially for joint 3D velocity inversions, offering more degrees of freedom compared to the 1D problem, this can lead to a systematic bias between the V_P and V_S (or V_P/V_S) solutions. The reliability of the solution-quality assessment is also limited, since detection of blunders in the joint data becomes rather impossible in the 3D case and undetected outliers may introduce significant artifacts in the tomographic models.

Due to the potential coupling between V_P and V_S solutions, the joint inversion for upper-crustal structure, where lithology dominates over pressure and temperature effects, is therefore disadvantageous from a petrophysical point of view. If *P* and *S* ray coverage is comparable and hypocenters are independently constrained by *P* as well as *S* data, the preferred strategy should thus be to start with the independent inversion of *P* and *S* data. This

strategy results in self-consistent models, allowing for an independent data-quality control as well as an unbiased assessment of damping parameters, model resolution, hypocenter accuracy, and petrophysical properties. The consistency of *P* and *S* data and the derived models can be assessed from differences in common hypocenters of the independent inversions. If differences are small compared to the spacing of the tomographic inversion grid or differences are comparable with uncertainties due to other error sources (anisotropy effects, ray-tracer accuracy, etc.), an additional joint inversion likely provides no benefit. Only if the differences in hypocenters of the independent inversions approach the grid-space dimension, the joint inversion (using the quality-filtered data and the results of the independent inversions as initial parameters) indeed provides additional constraints for the source-side velocity structure. In the case of the Central Alps region, *S* arrival-time data nowadays approach the quality and quantity of *P* data, and are sufficient for an independent inversion of the *S* data. In this study, we will therefore perform independent inversions of *P* and *S* data and demonstrate that the derived V_P and V_S models are of comparable resolution and provide consistent earthquake locations when combined in the hypocenter inversion.

The processing strategy applied in this study is summarized in Figure S2 and is described in detail in Sections 3 and 4. The key steps in the computation of highly accurate V_P and V_S models of the upper crust consist of several stages of minimum 1D inversions using the *VELEST* software (Kissling, 1988; Kissling et al., 1994), combined with different arrival-time quality filters. The initial *P* wave model used for the 1D inversion is based on the minimum 1D model of Husen et al. (2011). The initial model for the 1D *S* wave inversion is derived from the final 1D V_P values divided by an average crustal V_P/V_S ratio of 1.7. This average V_P/V_S ratio has been estimated from Wadati inversions (e.g., Kisslinger & Engdahl, 1973) in a previous study (Diehl et al., 2005; see Figure S3). The velocities and hypocenters derived by these independent 1D inversions are compared to results obtained from a joint 1D inversion of *P* and *S* data and used as initial values for the subsequent independent 3D local earthquake tomography (LET) inversion of V_P and V_S. The LET is performed using the *SIMULPS14* software (Eberhart-Phillips, 1990; Thurber, 1983) extended by a shooting ray tracer (Haslinger & Kissling, 2001) and the choice of inversion parameters is described in Section 4.

2.3. Consistent Relocation Procedure of Upper-Crustal Seismicity

To achieve accurate, absolute locations, including a realistic and consistent uncertainty estimate, the new *Pg* and *Sg* velocity models are used in combination with the NLL hypocenter location algorithm (Lomax et al., 2000, 2014). This algorithm is based on a probabilistic, nonlinear search method and is used with an *L*2-misfit function in this study. It allows the use of 1D or 3D velocity models (e.g., Husen et al., 2003) using the finite-difference forward solver of Podvin and Lecomte (1991), and it provides a full, nonlinear description of location uncertainties (see Section 2.1 and in the Supporting Information S1 for details). As described in Section 2.1, the probabilistic approach allows for incorporating Gaussian error estimates regarding velocity-model uncertainties (e.g., Lomax et al., 2000, 2014; Tarantola & Valette, 1982). We therefore assume the final root-mean-square (*RMS*) misfit of the tomographic inversions as typical error for travel times due to uncertainties of velocity models in the relocation procedure. In addition, topography corrections are applied to restrict the search volume to the half-space below the topography and therefore avoid locations above the free surface (Lomax et al., 2000, 2014).

To ensure consistent hypocenter estimation for the entire relocated catalog, we apply a quality-check and dynamic phase-selection procedure prior to the actual hypocenter inversion with NLL (see Figure S4 for details on parameters). In a first step, arrival times are predicted for the bulletin hypocenter using the new *Pg* and *Sg* 3D models. If the difference between prediction and actual manual bulletin pick exceeds the predefined thresholds, the bulletin pick is considered to be an outlier (e.g., due to clock error of instrument or erroneous pick) and will be ignored for the relocation. Considering the results of Figure 3, *P* and *S* phases passing the quality criteria are selected up to a maximum distance of 60 km (*P*) and 40 km (*S*) in a second step. Phases beyond these distances are only included until the minimum location quality criteria (number of observations and azimuthal gap) are fulfilled. The maximum distance considered is 120 km (*P*) and 60 km (*S*; see Figure 3c). In a final quality check, we inspect all *P* and *S* wave arrival-time residuals of the relocated hypocenters for systematic differences to ensure compatibility between the independently derived 3D V_P and V_S models.

3. High-Quality Arrival-Time Data for the Central Alps Region

3.1. Arrival-Time Data for Local Earthquake Tomography

The earthquake bulletin of the SED (*SEDBUL* catalog) provides the base of this dataset. Each arrival-time pick is manually revised and provided with an uncertainty estimate as defined in Table S1 in Supporting Information S1 and summarized in Husen et al. (2011). Since 2005, routine arrival-time picking procedures follow the guidelines described by Diehl, Kissling, Husen, and Aldersons (2009) and Diehl et al. (2012) to ensure consistency of manual picks. Since 1996, all events of $M_L \geq 2.5$ have been additionally quality checked and in most cases re-picked and complemented with data of other networks by the same two senior seismologists (e.g., Deichmann et al., 2000; Diehl et al., 2018). This review procedure results in a high level of consistency for events relevant for tomographic studies. To benefit from the quality of modern data of the SED, only earthquakes occurring between 1996 and April 2020 have been considered for the tomographic inversion. Since 2008, a significant portion of waveforms in the Central Alps region are shared among seismic networks in real-time and are integrated in the *SEDBUL* catalog. For an overview of currently available networks, see, for example, Diehl et al. (2021) and Hetényi et al. (2018). To further improve the data coverage for regions outside Switzerland before 2008, the *SEDBUL* data have been systematically complemented by data of Diehl, Kissling, Husen, and Aldersons (2009), including high-quality, manual and automatic *P* wave arrival times recorded at stations in the greater Alpine region (*DKHA* catalog). Figure 1a shows all seismic stations used in this study.

Initially, we selected earthquakes with *nobs* ≥6 and *gap* <180°, located within the boundaries 5.25°E–11.5°E and 45.0°N–48.5°N from the catalogs. To ensure the maximum number of crossing rays at upper-crustal levels, the entire focal-depth range was selected, including mid and lower-crustal seismicity present in the northern foreland of the Central Alps (asterisks in Figure 1b; e.g., Deichmann, 1992; Singer et al., 2014). These deep crustal earthquakes contribute near-vertical *Pg* and *Sg* rays and therefore help to constrain the velocity structure of the upper crust. In addition, we selected well constrained quarry blasts (*nobs* ≥ 8, *gap* < 180°, depth ≤ 3.0 km, and *mdi* ≤5.0 km), which were treated as earthquakes for tomographic inversion. This means that hypocenters of blasts were not fixed in the coupled inversion in order to realistically assess the GT accuracy of shallow seismic sources later. Arrival times in the *SEDBUL* data were complemented by data of the *DKHA* catalog. To remove redundant information, for example, from earthquake sequences, we performed a spatial de-clustering of the merged dataset on a 2.5 km × 2.5 km × 2.5 km grid. For this, we calculated a location-quality score based on location parameters, such as *nobs*, *gap*, and *mdi* for each event in a grid cell and selected the 10 events with the highest score to be considered for tomographic inversion. In addition, all earthquakes of $M_L \geq 3.3$ were selected irrespective of their score.

3.2. Quality-Control and Phase Selection for Tomography

Several stages of quality filtering were applied to ensure that arrival-time data are not contaminated by outliers due to erroneous picks, phase misidentifications, or clock errors caused, for example, by GPS problems (e.g., Diehl, Kissling, Husen, & Aldersons, 2009). All filters are based on event-location *RMS* (RMS_{event}) or arrival-time residuals (δ) derived by minimum 1D inversions (see Text S3 and Figure S2 for further details). All inversions were separately performed for *P* and *S* datasets. After an initial minimum 1D inversion, all residuals 0.4 s < $|\delta| \leq 3.0$ s were visually checked by comparison with the original seismogram using a semi-automated procedure and erroneous and questionable picks were removed from the data.

In a next step, *Pg* and *Sg* phases were dynamically selected (see Figure 3c). Phases at epicentral distances from 80 to a maximum of 140 km are considered only until the minimum location quality (*gap* < 170° and *nobs* ≥ 10) is reached. After another minimum 1D inversion, arrivals associated with events of suspiciously high RMS_{event} ($RMS_{event} > 2RMS_{final}$, where RMS_{final} is the overall, final *RMS* of the minimum 1D inversion) were visually checked. Erroneous and questionable picks were removed from the dataset.

During the last quality-filter stage, we performed statistical tests to assess the plausibility of remaining minimum 1D arrival-time residuals $|\delta| > 0.4$ s (i.e., residuals larger than the largest accepted error interval). To decide whether or not such residuals are associated with "real" earth structure rather than data blunders, we check the consistency with other residuals in the dataset. The proposed residual-consistency-check (*RCC*) assumes that a suspiciously large residual is likely related to true 3D anomalies, if similar ray paths show similar residual

amplitudes. The *RCC* filter is described in detail in Text S3 and Figure S2. All residuals $|\delta l| > 0.4$ s failing the *RCC* filter were removed. Finally, we removed all events with $gap > 180°$ and $nobs < 6$ after the *RCC* filtering.

4. Results

4.1. *Pg* and *Sg* Minimum 1D Model of the Central Alps Region

The final, quality-checked *Pg* dataset contains 63,532 phases of 4,605 events with an average assigned picking uncertainty of 0.063 s (see Table S1 in Supporting Information S1). This dataset largely benefits from massively improved station density in the Central Alps region since about 2010 and is therefore about six times larger than previous tomographic datasets (e.g., Diehl, Kissling, Husen, & Aldersons, 2009; Husen et al., 2003, 2011). At the same time, the average assigned picking uncertainty is about 0.04 s lower compared to previous studies. This corresponds to a potential improvement of about 40% in terms of the smallest resolvable velocity anomaly in the upper crust. The final minimum 1D inversion was performed following the procedure described in Section 2.2. The inversion converges within four iterations and the final *RMS* is 0.084 s. Figure 4a shows the derived 1D *Pg* velocity profile and the depth distribution of hypocenters resulting from the coupled inversion. The depth range between 0 and 14 km is well constrained by *Pg* phases of upper-crustal seismicity. Deeper parts of the 1D model are mainly resolved by mid to lower-crustal seismicity in the northern Alpine foreland. Since the lower-crustal seismicity can have *Pn* cross-over distances <80 km (e.g., Singer et al., 2014), we cannot exclude that a few *Pn* phases are included in our dataset in the northern Alpine foreland. The Moho first-order velocity discontinuity, however, is not resolved with this data. As expected, resolution below 30 km is certainly poor but this depth range is not the target of this study.

Figure 4d shows the corresponding minimum 1D station corrections, which are largely consistent with previous results (Diehl, Kissling, Husen, & Aldersons, 2009; Husen et al., 2003, 2011). They are dominated by the velocity contrasts between Cenozoic sediments in the northern (Molasse basin) and southern (Po plain) foreland (positive delays) and Mesozoic and crystalline basement units in the Alps (negative delays). Examples for second-order anomalies in the Alpine domain are provided by the positive delays in eastern Switzerland, which have previously been associated with Bündnerschiefer (calcschists) sediments or local site effects caused, for example, by sedimentary filling of Alpine valleys. The latter effect is clearly imaged by the densely instrumented Rhone valley in southwest Switzerland (Figure 4d).

The final, quality-checked *Sg* data contain 32,663 phases of 2,908 events with a formal average assigned picking uncertainty of 0.118 s (see Table S1 in Supporting Information S1). As expected for secondary arriving *S* waves, the assigned picking uncertainties are higher and the number of available phases lower compared to the *P* data. The initial *S* velocity model was derived from the *P* model of Figures 4a and a constant V_P/V_S ratio of 1.7 (see Section 2.2). The inversion converges within four iterations and the final *RMS* is 0.095 s. The fact that the final *RMS* is smaller than the average *Sg* picking uncertainty suggests that the assigned arrival-time uncertainties are likely too pessimistic (i.e., too large). The derived 1D velocity profile and focal-depth distribution is shown in Figure 4b, and corresponding station corrections are presented in Figure 4e. The general tendency (foreland vs. Alps) is remarkably consistent with the *P* corrections, though differences in sign exist in few regions, indicating possible lateral differences in the V_P/V_S ratio. Figure 4c documents the V_P/V_S ratio versus depth, derived from the individual *P* and *S* models. On average, the V_P/V_S ratio in the upper crust is close to or slightly below 1.7, coinciding with the value obtained by Wadati inversion. Although at the limit of data resolution, the 1D results suggest an increase in the V_P/V_S ratio in the lower crust. This increase agrees with other seismological studies and is indicative of a mafic composition of the lower crust (e.g., Christensen, 1996; Zandt & Ammon, 1995).

To ensure that velocity models and hypocenters derived by the independent inversion of *P* and *S* data are compatible and consistent, we compared them to results from a joint $V_P + V_S$ minimum 1D inversion. For this test, we selected 2,064 common events from the two independent datasets. Initial velocity models for the combined inversion are the independent models of Figure 4. We then initiated the combined inversion once from the hypocenters resulting from the independent *P* and once from the hypocenters resulting from the individual *S* inversion. Figure S5 shows the resulting 1D models in comparison with the independent models. Differences in the well-resolved parts are negligible, indicating that the individual inversions converge to the same minimum as the joint inversion. In addition, we assessed the differences in focal depth and epicenter between hypocenters derived from the independent *P* and *S* inversions in Figure 5a. The mean difference in focal depth is about −400 m (standard

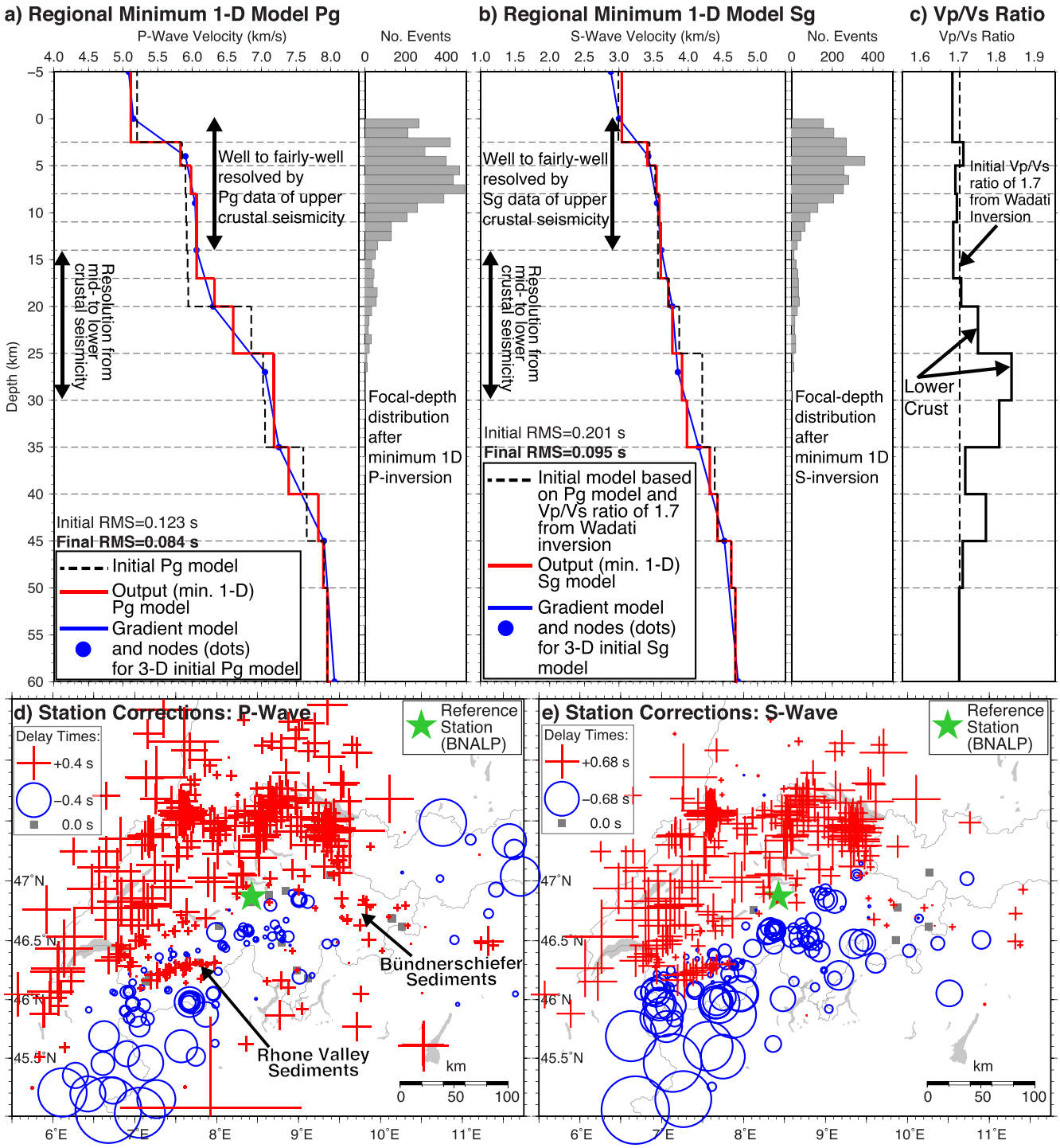

Figure 4. Minimum 1D models and focal-depth distributions derived from *Pg* and *Sg* arrival-time data. (a) Final (independent) *Pg* velocity model (red line) derived by coupled hypocenter-velocity inversion. (b) Final *Sg* velocity model (red line) derived by the independent inversion of *S* data. (c) Profile of V_P/V_S ratio derived from independent models shown in (a) and (b). (d) *Pg* station corrections corresponding to the *Pg* velocity model of (a). (e) Corresponding *Sg* station corrections. Only stations with ≥5 observations are shown in (d) and (e). Symbol size in (e) is scaled by 1/1.7 (i.e., the inverse of the average V_P/V_S ratio) to facilitate comparison between *Pg* and *Sg* corrections. Green star in (d) and (e) marks the location of reference station BNALP.

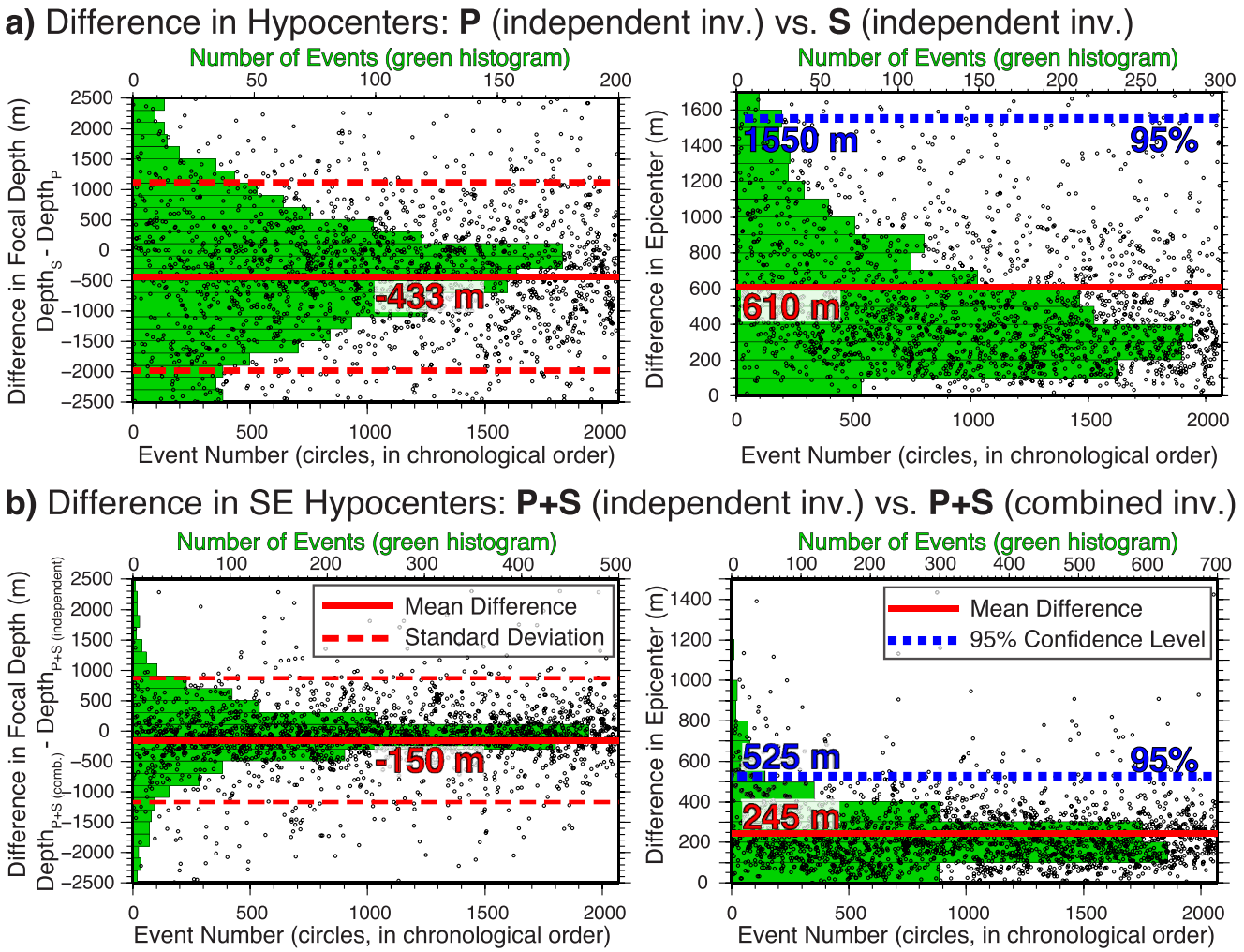

Figure 5. Differences in hypocenter locations derived by different minimum 1D inversion strategies for *P* and *S* data. Black circles indicate differences for individual hypocenters. Statistical distribution of differences is indicated by green histograms in the background. (a) Differences in focal depth (left) and epicenter (right) for hypocenters derived by independent minimum 1D inversions of *P* and *S* data for 2,064 well constrained hypocenters. Blue dotted line marks the difference in epicenter including 95% of all events. (b) Differences in focal depth and epicenter for the same hypocenters derived by single-event (SE) relocation using *P* and *S* minimum 1D models from independent and from combined (joint $P + S$) minimum 1D inversions.

deviation: ±1,500 m). The mean difference in epicenter location is about 600 m and 95% of the epicenters have differences ≤1,550 m. The relatively small differences in hypocenters therefore document the consistency between *P* and *S* arrival-times picks and the comparability in quality of the two datasets. In a second test, we relocated the 2,064 events with *P* and *S* arrivals in single-event mode using (a) the two individual V_P and V_S models (and corresponding station corrections) and (b) the V_P and V_S models from the joint $V_P + V_S$ inversion (and corresponding station corrections). The corresponding differences in hypocenters in Figure 5b are significantly smaller (mean difference in depth: −150 m with standard deviation ±1,000 m; mean difference in epicenter: 250 m with 95% of the epicenters having differences ≤525 m). Differences in hypocenters resulting from differences in the minimum 1D models are therefore close to (for focal depths) or smaller (for epicenters) than the targeted sub-kilometer accuracy and several times smaller than the 3D grid spacing used for the LET inversion (see Section 4.2). From this test we conclude that well-constrained hypocenters derived from the combination of independently inverted V_P and V_S models are consistent with results from joint inversion strategies for our high-quality dataset.

4.2. *Pg* and *Sg* 3D LET Model of the Central Alps Region

The results of the minimum 1D inversions were used as initial parameters for the 3D LET procedure described in Section 2.2. The corresponding 1D layer velocities were approximated by 1D gradient models (blue lines and dots in Figure 4). To find the best balance between homogeneous and continuous resolution over significant areas (as indicated, e.g., by uniformly distributed amplitudes of resolution-matrix diagonal elements) and highest possible image resolution (defined by grid spacing; e.g., Husen et al., 2003; Kissling et al., 2001), various model parametrizations have been tested. A good compromise was achieved by using a horizontal grid spacing of 10 km × 10 km and a vertical spacing of 4–5 km, resulting in an over-determination ratio (number of observations divided by number of model parameters) of 1.7 (*Pg*) and 1.1 (*Sg*). Optimal damping values were estimated from multi-iteration trade-off curves and synthetic recovery tests as described in Supporting Information S1. Based on these tests, we selected damping values of 100 (*Pg*) and 150 (*Sg*) in combination with five iterations for the LET inversion. The final weighted *RMS* values of the inversions are 0.069 s (variance reduction with respect to initial model: 81%) for *Pg* and 0.114 s (variance reduction: 87%) for *Sg*.

The amplitude recovery and the model resolution were assessed by a series of synthetic tests described in detail in Supporting Information S1. In addition, we assessed the spread of the full resolution matrix by resolution contours (Reyners et al., 1999) and the spread function (Michelini & McEvilly, 1991). Based on these tests, we associated diagonal elements of the resolution matrix (RDE values) ≥0.075 with well to fairly well resolved regions of the 3D V_P and V_S models. Our results are consistent with definitions used in other LET studies (e.g., Eberhart-Phillips & Reyners, 2012; Lin et al., 2007, see Supporting Information S1 for details). We therefore define $RDE = 0.075$ in all following tomographic images as the boundary between well to fairly well resolved and poorly to unresolved parts of the model. As documented in Figures S8 and S9 in Supporting Information S1, resolution of synthetic structures at 0 km depth is mainly restricted to NE and SW Switzerland, the two regions with the highest density of seismic stations. Resolution is rather homogeneous for the entire study region at 4 km depth. At 9 km, most of the synthetic structures are still well recovered. However, we observe vertical leakage from high-velocity anomalies located at 4 km depth into this layer. Despite the smaller number of *S* data, the resolution is remarkably similar to *P* for the center parts of the study region. This similarity suggests that the additional data available for *P* contain mostly redundant ray paths, which increase the resolution only marginally compared to that based on *S* alone. This equivalence in resolution therefore justifies the independent inversion of both datasets and the subsequent comparison, for example, in terms of 3D variations of V_P/V_S ratios.

Figures 6 and 7 show horizontal sections of the obtained V_P and V_S models in terms of relative changes with respect to the 1D reference velocities for layers located at 0, 4, and 9 km depth. One of the first-order features resolved in the uppermost layer at 0 km (sensitive depth range: −2.5–2 km, where negative depth corresponds to elevation above sea level) are the high velocities in an area where the European Crystalline basement crops out, or is at very shallow depth between only −250 and +250 m depth in respect to sea level (*H*1 in Figures 6a and 7a). This anomaly contrasts with the low velocities found in an adjacent band to the south (*L*1 in Figures 6a and 7a), comprising Cenozoic, Mesozoic, and Permo-Carboniferous sediments of the northern Molasse Basin (NMB). Another close match with surface geology is imaged between the southeastern boundary of the NMB and the Alpine front in northeastern Switzerland (*L*2 and *H*2 in Figures 6a and 7a). Here, and also along large portions of that contact further SW and along strike, the contrast between lower and higher V_P and V_S velocities correlates precisely with the tectonic boundary between the Cenozoic sediments of the Subalpine Molasse, whose base is far below 2 km depth and which are overthrusted by the sedimentary units of the Helvetic nappes. The area of the limestone dominated Helvetic nappes and the External Crystalline Massifs is characterized mainly by an increase in V_P and partially also in V_S (*H*2–*H*4 in Figures 6a and 7a). The Plio-Pleistocene fill of Alpine valleys such as the Rhone valley in southwest Switzerland (*L*3 in Figures 6a and 7a) are characterized by low V_P and V_S values.

A prominent feature in the horizontal section at 4 km depth (sensitive depth range: 2–6.5 km) is the relative broadening of the band of low velocities associated with the NMB toward the Alps when compared to the 0 km section (Figures 6b and 7b). The V_P and V_S low-velocity anomalies extend toward the southeast across the Alpine front, which reflects the fact that the Subalpine Molasse units extend southward over considerable distance below the basal thrust of the Helvetic nappes (Figures 6b and 7b). The areas of outcropping crystalline basement in the foreland (e.g., Black Forest Massif) and in the Alps (e.g., external Aar Massif) only denote a slight increase in V_P (about 0% to +2%), whereas V_S shows a relatively greater increase (about +2% to +5%, e.g., in the Black Forest Massif). In the Alps and especially along the Aar Massif, V_S is even higher and an increase of about +5% to +7%

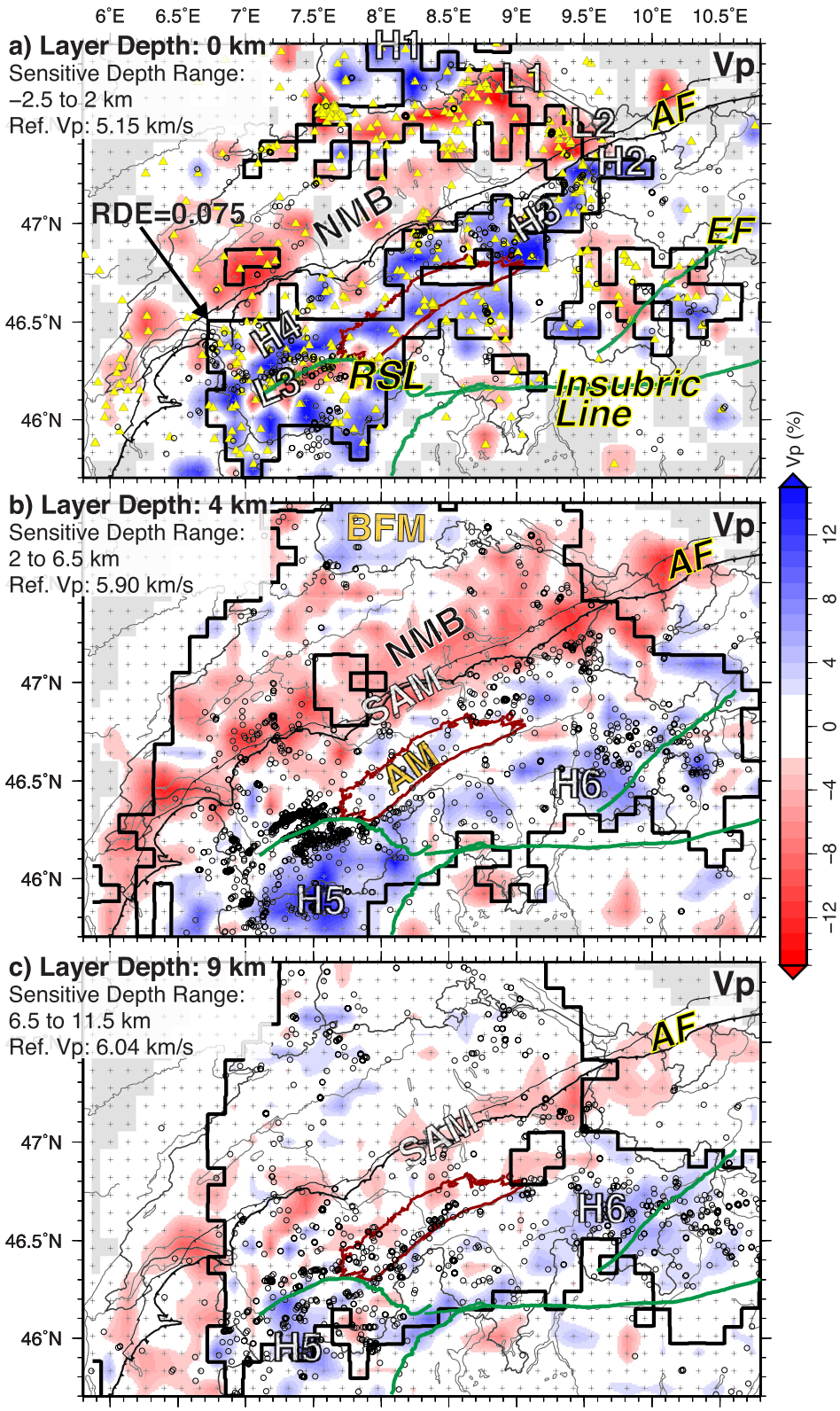
6°E
6.5°E
7°E
7.5°E
8°E
8.5°E
9°E
9.5°E
10°E
10.5°E
a) Layer Depth: 0 km
Sensitive Depth Range:
−2.5 to 2 km
Ref. Vp: 5.15 km/s
Vp
H1
L1
L2
AF
H2
RDE=0.075
NMB
H3
EF
47°N
46.5°N
46°N
H4
L3
RSL
Insubric
Line
b) Layer Depth: 4 km
Sensitive Depth Range:
2 to 6.5 km
Ref. Vp: 5.90 km/s
BFM
Vp
AF
NMB
SAM
AM
H6
H5
c) Layer Depth: 9 km
Sensitive Depth Range:
6.5 to 11.5 km
Ref. Vp: 6.04 km/s
Vp
AF
SAM
H6
H5
Vp (%)
12
8
4
0
−4
−8
−12

Figure 6.

(locally >+7%) is observed (Figures 6b and 7b). The Penninic nappes generally correlate with increased V_P and V_S values at 4 km depth (*H5*–*H6* in Figures 6 and 7b). These increased velocities might be related to crystalline basement units within the Penninic nappes.

In the 9 km depth section (Figures 6c and 7c), the amplitudes of velocity variations generally decrease and anomalies become more discontinuous. The velocities in the basement of the northern foreland appear rather uniform. Reduced V_P is mainly observed along the frontal area of the Alps, whereas increased V_P is restricted to the Penninic realms. However, as shown by the synthetic test in the Supporting Information S1, vertical leakage from overlying high-velocity anomalies cannot be excluded in this area.

4.3. Consistent Relocation of Seismicity in the Central Alps

The 3D V_P and V_S models were interpolated on a 1 × 1 × 1 km grid to provide accurate travel-time tables for the relocation procedure. The final *RMS* of 0.069 s of the V_P model was assumed as a Gaussian error estimate of velocity-model uncertainties in all relocations. The relocation procedure described in Section 2.3 was calibrated and tested for several well-studied earthquake sequences and quarry blasts, which were considered as GT events.

The induced St. Gallen sequence of 2013 (Figure 1b), caused by stimulation operations of a geothermal project (e.g., Diehl et al., 2017), represents such a sequence for GT testing. The induced seismicity was monitored by a dense seismic network and accurate local *P* and *S* minimum 1D models were derived from about 100 high-quality events (Diehl et al., 2017). Additionally, these results were calibrated with a model from a 3D reflection seismic survey (Heuberger et al., 2016). Using the local minimum 1D models, the accuracy of the absolute hypocenter location was estimated to be about ±100 m at the epicenter and ±150 m in focal depth (Diehl et al., 2017). Gray and red dots in Figures 8a–8c show the hypocenters of Diehl et al. (2017) and considered as GT locations. Black circles in Figures 8a and 8b show the corresponding hypocenters derived with the NLL algorithm in combination with the new velocity models. Figure 8a shows the hypocenters derived with the regional minimum 1D model of Figure 4. Although the regional minimum 1D model provides rather homogeneous locations with geometries similar to the GT results, the hypocenters are systematically shifted toward the NW by about 0.4 km and more than 1 km shallower when compared to the GT locations. The derived results would therefore lead to a wrong interpretation regarding the location and/or type of the reactivated fault segment.

Figure 8b shows the results achieved with the regional 3D model, which results in a cluster centroid close to the GT solution (in epicenter and depth). The 3D model leads, on the other hand, to a stronger scatter of hypocenters compared to the 1D model approach. These scattered locations, however, are mainly associated with less constrained hypocenters. This scatter in hypocenters can be significantly reduced by subsequent double-difference relative relocation in combination with cross-correlation differential times as demonstrated in Figure 8c. For this, we used the absolute locations derived by the 3D model approach (Figure 8b) as initial locations for the *hypoDD* double-difference algorithm of Waldhauser and Ellsworth (2000). The resulting double-difference epicenters are within 100 m and focal depths within 200 m from the GT solutions (Figure 8c). For the bulk of hypocenters derived with the regional 3D model approach, the formal 1σ uncertainties (yellow ellipses and gray error bars in Figure 8b) provided by the NLL algorithm are realistic, that is, they include the GT location. The 1σ horizontal uncertainties are too optimistic (i.e., do not include the GT location) only for 10% of the epicenters in Figure 8b. About 43% of the focal-depths uncertainties do not include the GT depth. For these cases, the average difference between the GT depth error and the NLL depth uncertainty is only about 100 m and therefore within the ±150 m uncertainty of the GT depths. In the case of the regional 1D model approach (Figure 8a), the formal 1σ uncertainties are not representative for the hypocenter accuracy, especially regarding focal depths.

Accuracy and precision of the regional 3D model approach were also assessed by selected quarry-blasts. Figures 8d–8f document the improvement in terms of accuracy (i.e., absolute location) and precision (i.e., reduced

Figure 6. Tomographic 3D $\%V_P$ model derived from the independent inversion of *Pg* phases. The velocity structure is shown as percentage change relative to the 1D initial reference models of Figure 4. Results are displayed in horizontal sections at depths of 0, 4, and 9 km sensitive in the indicated depth ranges. Bold black contours include areas that are well and fairly well resolved (RDE ≥ 0.075); areas outside these contours have poor resolution. Gray areas correspond to regions with derivative-weighted sum (DWS) values <5 that are not resolved at all. White areas correspond to velocity anomalies below the significance level (−2%–+2%). Yellow triangles indicate seismic stations contributing to the tomographic inversion. Circles mark contributing earthquakes located within the corresponding depth interval. Dark red line shows the outline of the Aar Massif (AM) exposed at the surface. AF, Alpine Front; BFM, Black Forest Massif (European crystalline basement); EF, Engadine fault; NMB, Northern Molasse Basin; RSL, Rhone-Simplon line; SAM, Subalpine Molasse. High (H1–H6) and low (L1–L3) velocity anomalies are discussed in text.

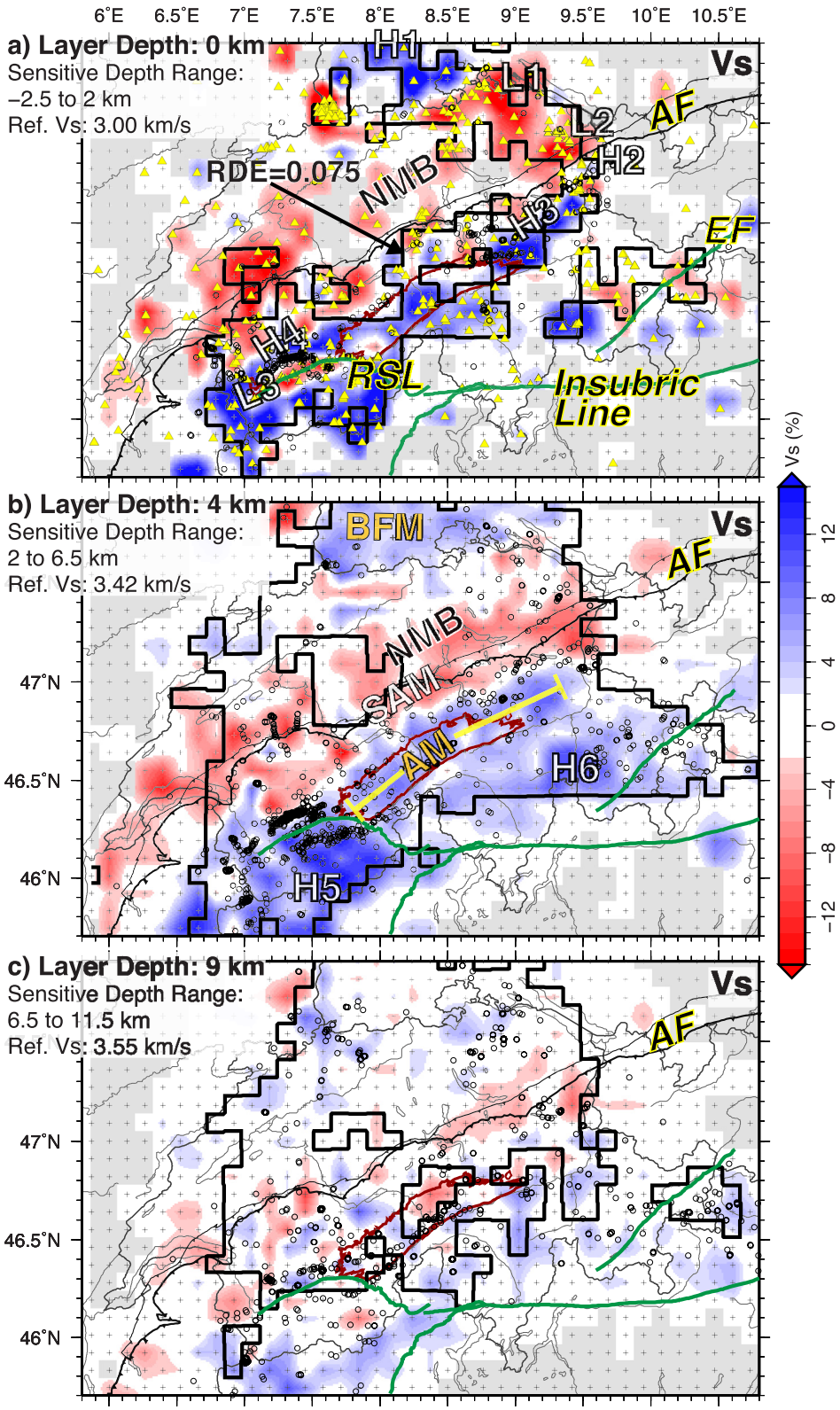

Figure 7. Tomographic 3D $\%V_S$ model derived from the independent inversion of *Sg* phases. The velocity structure is shown as percentage change relative to the 1D initial reference models of Figure 4. Results are displayed in the same way as the V_P model in Figure 6. AF, Alpine Front; AM, Aar Massif; BFM, Black Forest Massif (European crystalline basement); EF, Engadine fault; NMB, Northern Molasse Basin; RSL, Rhone-Simplon line; SAM: Subalpine Molasse. High (H1–H6) and low (L1–L3) velocity anomalies are discussed in text.

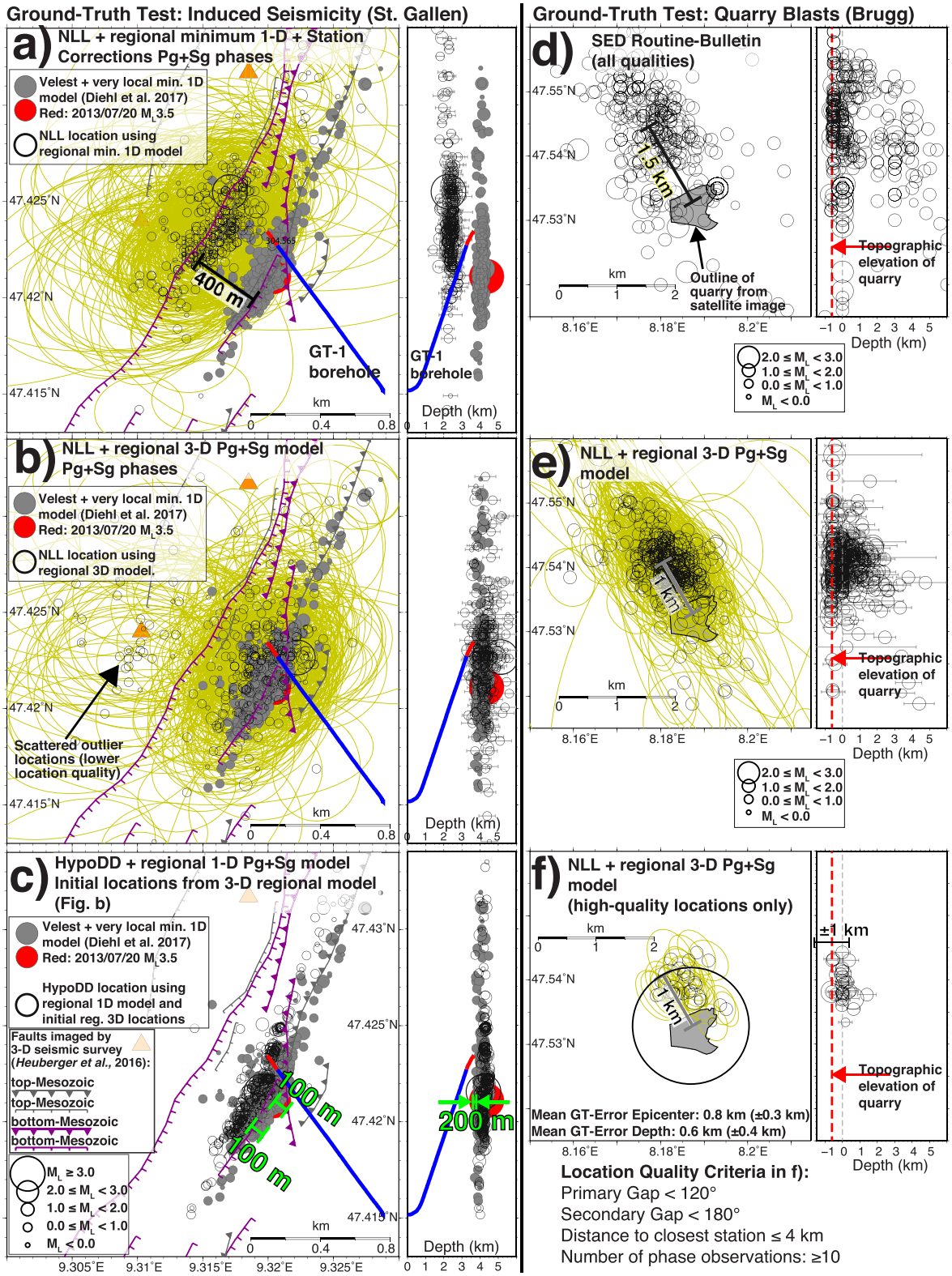
Ground-Truth Test: Induced Seismicity (St. Gallen)
a) NLL + regional minimum 1-D + Station Corrections Pg+Sg phases
Velest + very local min. 1D model (Diehl et al. 2017)
Red: 2013/07/20 M_L 3.5
NLL location using regional min. 1D model
400 m
GT-1 borehole
b) NLL + regional 3-D Pg+Sg model Pg+Sg phases
Velest + very local min. 1D model (Diehl et al. 2017)
Red: 2013/07/20 M_L 3.5
NLL location using regional 3D model.
Scattered outlier locations (lower location quality)
c) HypoDD + regional 1-D Pg+Sg model Initial locations from 3-D regional model (Fig. b)
Velest + very local min. 1D model (Diehl et al. 2017)
Red: 2013/07/20 M_L 3.5
HypoDD location using regional 1D model and initial reg. 3D locations
Faults imaged by 3-D seismic survey (Heuberger et al., 2016):
top-Mesozoic
top-Mesozoic
bottom-Mesozoic
bottom-Mesozoic
100 m
100 m
200 m
Depth (km)
Ground-Truth Test: Quarry Blasts (Brugg)
d) SED Routine-Bulletin (all qualities)
1.5 km
Outline of quarry from satellite image
Topographic elevation of quarry
2.0 ≤ M_L < 3.0
1.0 ≤ M_L < 2.0
0.0 ≤ M_L < 1.0
M_L < 0.0
e) NLL + regional 3-D Pg+Sg model
1 km
f) NLL + regional 3-D Pg+Sg model (high-quality locations only)
±1 km
Mean GT-Error Epicenter: 0.8 km (±0.3 km)
Mean GT-Error Depth: 0.6 km (±0.4 km)
Location Quality Criteria in f):
Primary Gap < 120°
Secondary Gap < 180°
Distance to closest station ≤ 4 km
Number of phase observations: ≥10

Figure 8.

scatter) for blasts at a quarry in the Alpine foreland. Compared to the original SED bulletin locations, the centroid of blasts resulting from relocation with the regional 3D model approach locates about 0.5 km closer to its GT position and scatter of hypocenters (in epicenter as well as depth) is significantly reduced (Figures 8d and 8e). Although a systematic shift toward the NW remains after relocation, sub-kilometer accuracy in epicenter and depth is reached for about 60% of the high-quality solutions in Figure 8f (mean error in epicenter: 0.8 km and depth: 0.6 km). Of all solutions in Figure 8e, about 39% of the formal 1σ horizontal uncertainties include the GT epicenter and about 43% of the 1σ depth uncertainties include the GT depth. These results suggest that the 1σ uncertainties of NLL can be too optimistic for such blast locations and possibly underestimate errors in the shallowest part of the velocity model.

Finally, the regional 3D model procedure was applied to the entire instrumental catalog of the SED for earthquakes and identified explosions located in the box labeled *ECOS09* in Figure 1a for the period of January 1984–May 2020. In total, 20,201 earthquakes and 3,644 explosions (mainly quarry blasts) have been relocated. Due to insufficient numbers of observations passing the selection and quality criteria, relocation failed for a subset of solutions, mainly events from the early period of the instrumental catalog. The final relocated catalog contains 18,794 earthquakes and 3,010 explosions. To ensure the compatibility of the independently derived 3D V_P and V_S models, we have checked the final arrival-time residuals resulting from the NLL relocation for systematic differences between *P* and *S* phases in Figure S12. The differences in the mean values are 0.02–0.03 s for observation-quality classes 0–3. These differences are in the range of the smallest assigned picking uncertainty (±0.025 s) and significantly below the average assigned picking uncertainties of both datasets. From this analysis we conclude that no significant systematic offset is present in the arrival-time residuals and that the individual 3D models provide consistent locations when combined in the hypocenter inversion. Figure 9 summarizes first-order location-quality parameters of the relocated catalog for two time periods. Hypocenter qualities considerably improve after 2010 due to the densification of the seismic network. Uncertainties in epicenter and focal depth for hypocenters in this period are mostly within the targeted sub-kilometer range.

Figure 10a shows the relocated catalog for upper-crustal earthquakes (focal depth ≤15 km) of minimum location quality (*gap* < 200° and *nobs* ≥ 6) in the Central Alps region. The improvement in accuracy and precision of the relocated catalog is documented for one region in more detail. Figure 10b shows the SED bulletin locations of an earthquake sequence, which occurred north of the Rhone-Simplon Line (RSL) in 2019 and 2020. The bulletin locations scatter significantly and several events of larger magnitudes locate to the southeast, apparently disconnected from the main cluster. Relocated seismicity in Figure 10c shows an overall reduction in scatter and the events of larger magnitudes moved about 0.7 km toward the northwest and locate, as expected, in the center of the cluster. After relocation, the absolute locations image an ENE-WSW striking fault, consistent in orientation with the dextral plane of the focal mechanism of an M_L 3.2 earthquake (Figure 10c). Additional examples documenting the improvement of the relocated catalog will be discussed in the following sections.

5. Discussion

5.1. Inversion Strategies Combining *Pg* and *Sg* Phases to Achieve Accurate Hypocenters

The results presented in Section 4.1 document that comparable, high-quality datasets of *P* and *S* arrivals lead to virtually identical minimum 1D V_P and V_S models irrespective of the chosen inversion strategy (i.e., independent vs. joint models). The differences in hypocenter location resulting from differences in the corresponding velocity models are within the targeted sub-kilometer accuracy and therefore considered negligible in our case. In comparison with the grid spacing of 10 km × 10 km × 5 km and an average horizontal ray length of about 40 km used in our tomographic inversion, these differences are also insignificant in respect to their impact on the 3D velocity

Figure 8. Ground-truth (GT) assessment of hypocenter accuracy and precision using the induced seismicity related to the geothermal project near St. Gallen (left-hand column, see Figure 1b for location) and blasts from a quarry near Brugg in northern Switzerland (right-hand column). Left: Gray dots indicate the hypocenters derived with a local minimum 1D model using the *VELEST* software (Diehl et al., 2017), which are considered as GT locations. Black circles in (a) and (b) indicate the solutions derived with the *Nonlinloc* (NLL) algorithm in combination with different regional velocity models and dynamic phase selection. (a) Hypocenters derived with the regional minimum 1D model of Figure 4. (b) Hypocenters derived with the regional 3D model of Figures 6 and 7. (c) Double-difference relative relocations using the NLL locations shown in (b) as initial hypocenters. Right: (d) SED bulletin locations of quarry-blast locations. (e) Relocated blasts using NLL in combination with the new 3D *Pg* and *Sg* velocity models and dynamic phase selection. (f) Same as (e) but only showing high-quality locations (quality parameters listed in figure). Yellow ellipses and gray bars correspond to horizontal and vertical 1σ uncertainties (68% confidence level) derived by the NLL algorithm. Note that the depth scales on the vertical cross-sections are greatly compressed relative to the map scale.

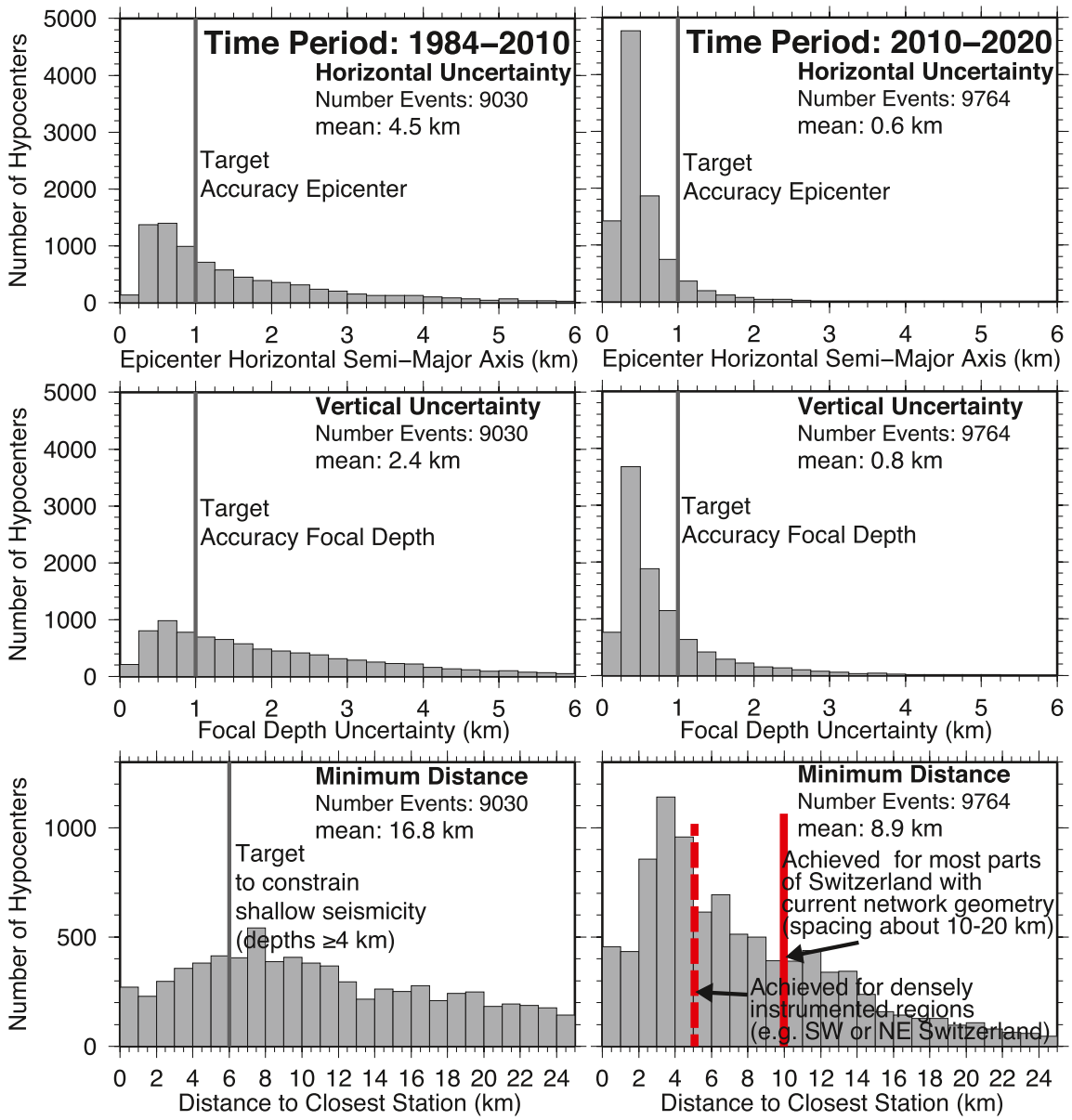

Figure 9. Statistics of location qualities (horizontal and vertical uncertainties as provided by the *Nonlinloc* (NLL) algorithm, distance to the closest observing station) of the relocated Swiss Seismological Service (SED) bulletin divided into two time periods. Left-hand column: Earthquakes occurring between 1984 and 2010. Right-hand column: Earthquakes between 2010 and May 2020. Improvement in network density and quality of seismic instruments since about 2010 results in significantly reduced location uncertainties, achieving sub-kilometer precision for the majority of relocated seismicity in this period. Mean distance to closest observing stations as well as modeled minimum distance (vertical red lines, see Figure S13b for details) suggest that focal depth is well constrained for the majority of seismicity with the current network geometry.

structure. The consistency between *P* and *S* arrivals-time residuals of the relocated catalog (Figure S12), on the other hand, indicates that the derived 3D V_P and V_S models are also compatible when combined in single-event hypocenter determination. This procedure, however, requires consistently picked *P* and *S* arrivals, hypocenters independently constrained by *P* as well as *S* data and an accurate estimate of the average crustal V_P/V_S ratio (e.g., from Wadati inversion). In addition, differences between *P*- and *S*-based hypocenters as well as travel-time residuals need to be assessed to ensure that the independent models result in consistent hypocenter locations when combined in the relocation procedure. The independently derived 3D V_S model, on the other hand, provides the advantage that it is decoupled from the V_P model and independent from *a priori* assumptions on the coupling

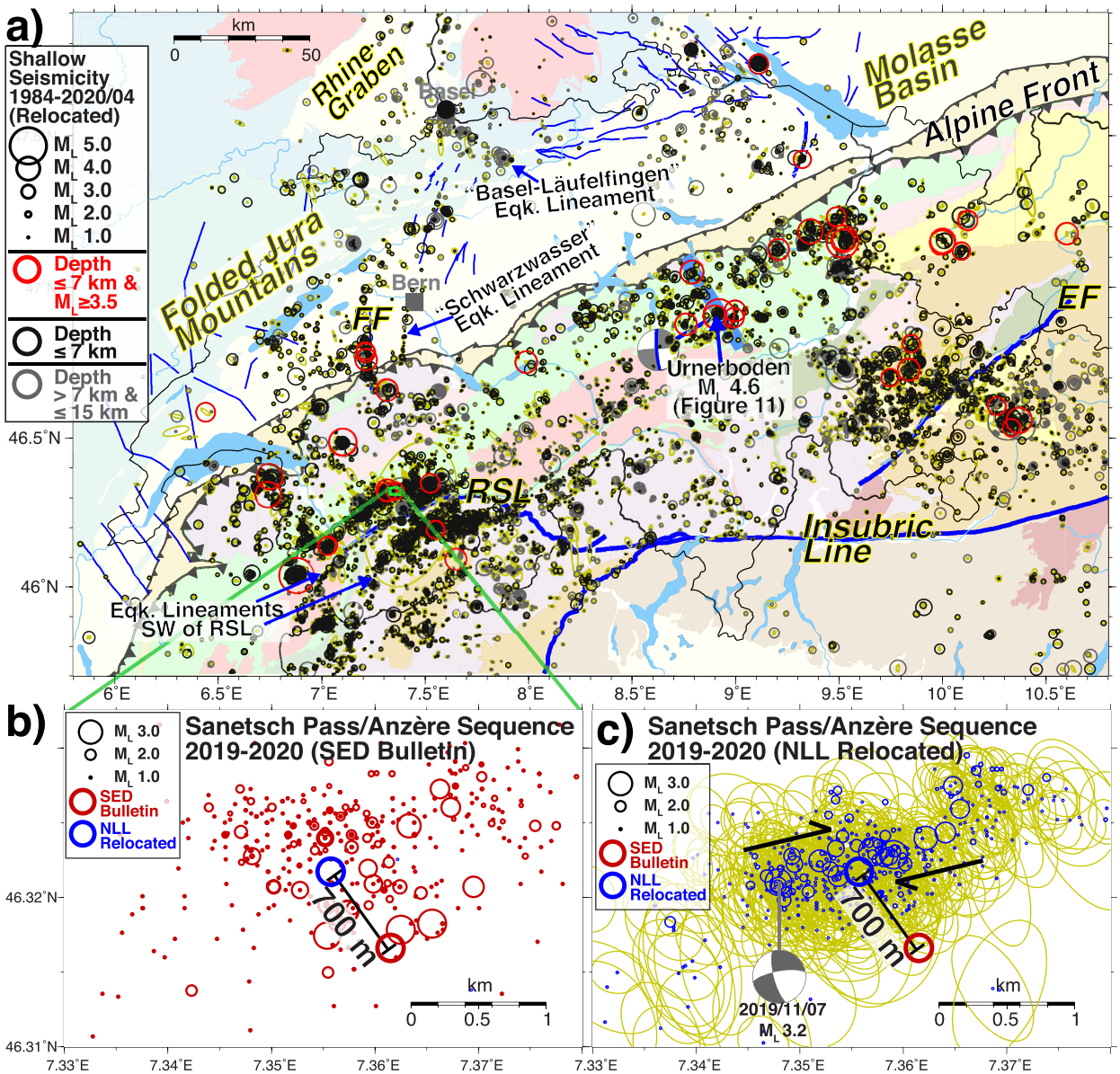

Figure 10. Relocated earthquake catalog for the Central Alps for the period 1984/01 to 2020/05 and comparison to previous Swiss Seismological Service (SED) bulletin locations. Only upper-crustal earthquakes (focal depth ≤15 km) with minimum location-quality criteria (*gap* < 200° and *nobs* ≥ 6) are shown. Yellow ellipses correspond to horizontal uncertainties (68% confidence level). (a) Absolute relocations of seismicity in the Central Alps and their northern foreland. See Figure 1b for description of tectonic units and faults. Blue line marks the location of the cross-section shown in Figure 11. (b) SED bulletin hypocenters (red circles) of seismicity north of the RSL between 2019 and 2020, including the Sanetschpass/Anzère sequence of November 2019. (c) Absolute relocations (blue circles) derived in this study for the sequence shown in (b).

between V_P and V_S. In addition, this strategy allows for an unbiased assessment of the model resolution and therefore provides self-consistent solutions of the 3D V_P and V_S field.

The results of the tomography in Figures 6 and 7 document significant 3D variations of V_P and V_S in the upper crust of the Central Alps and their foreland. Structures are imaged at unprecedented resolution compared to previous studies (e.g., Diehl, Husen, Kissling, & Deichmann, 2009; Husen et al., 2003) and, as described in Section 4.2, correlate to first order with major tectonic units of the Central Alps region. Although the overall V_P and V_S structures are remarkably similar, differences exist, indicating variations in the V_P/V_S ratio in some regions. A prominent example is the Aar Massif, where the relative increase in V_S is higher than the one in V_P, indicating a below-average V_P/V_S ratio (Figures 6b, 7b, and 11). In conclusion, the observed variations in V_P, V_S, and V_P/V_S

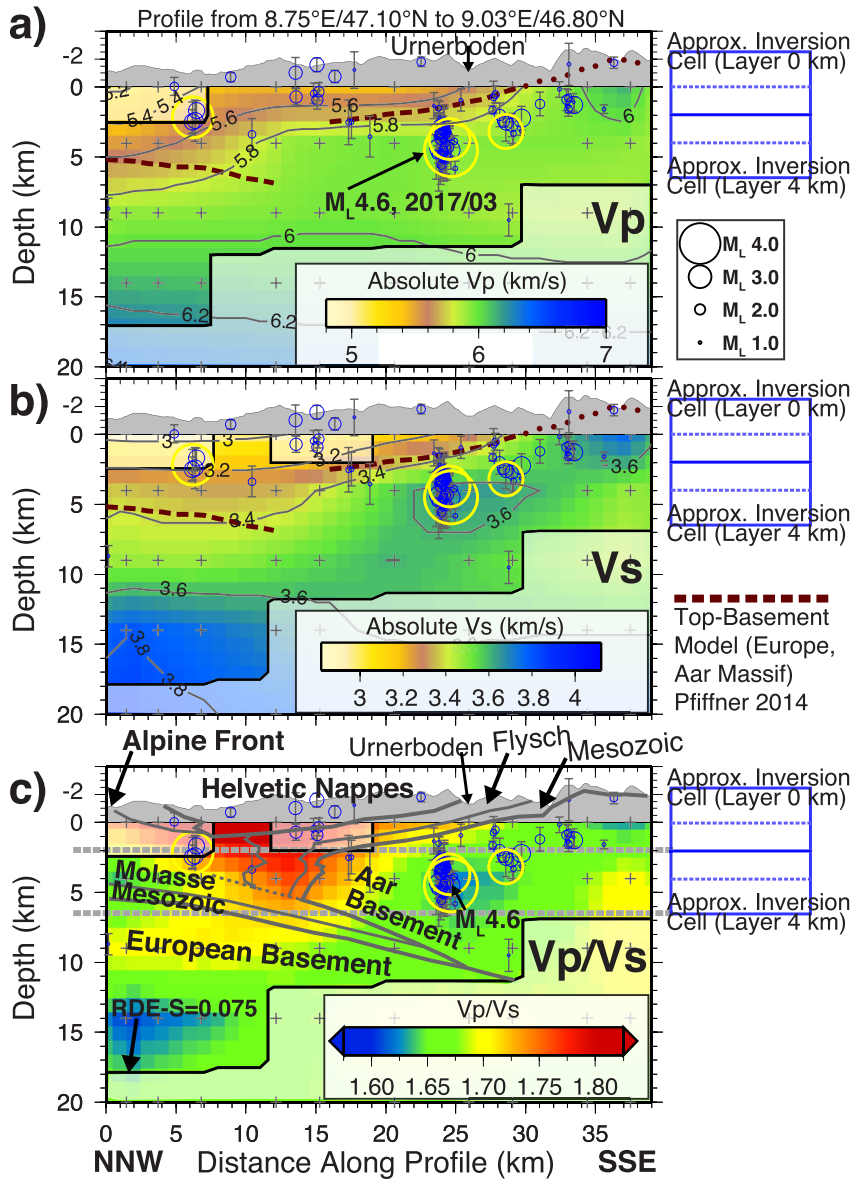

Figure 11. Three versions of a vertical transect across the source region of the M_L 4.6 Urnerboden earthquake of 2017. The location of the transect is shown in Figure 10a. (a) Cross-section showing the tomographic V_P model. Colors and contour lines indicate absolute V_P. (b) Same cross-section across the V_S model. (c) Same cross-section showing the V_P/V_S ratio derived by division of values of independent V_P and V_S models. Gray lines indicate the geological interpretation (see text for details). Regions of poor resolution (*RDE* < 0.075) are masked. Crosses indicate nearby inversion nodes projected from either side onto the profile. Blue circles mark relocated seismicity projected within ±5 km from each side of the profile. Yellow circles mark events of $M_L \geq 3.5$. Only high-quality hypocenters are shown (*gap* < 180°, *nobs* ≥ 10, *mdi* ≤ 1.5 × focal-depth or *mdi* ≤ 20 km, focal depth precision ≤2 km, and location *RMS* ≤ 0.5 s). Gray error bars indicate 1σ focal-depth uncertainties. Blue rectangles to the right indicate the approximate sensitivity range of inversion nodes at 0 and 4 km depth.

evidence the need for velocity models accounting for these structures in order to achieve accurate hypocenters in the Central Alps region.

5.2. Hypocenter Accuracy and Precision of the *Pg-Sg* Relocation Procedure

Based on the results achieved for the St. Gallen case (Figures 8a–8c), we conclude that the most accurate and precise (i.e., least scattering) hypocenters are achieved by very local minimum 1D models, following procedures, for example, described by Diehl et al. (2017). However, computation of such local models is time-consuming and

only possible if the numbers of events and phases are sufficiently large. Synthetic tests and comparison with selected GT events performed in this study document that sub-kilometer hypocenter accuracy can be also achieved with the proposed *Pg*-*Sg* relocation procedure in combination with accurate, regional 3D velocity models for densely instrumented networks. The St. Gallen case, however, suggests that the 3D velocity structure can also result in an increased level of scatter for less well-constrained solutions in comparison to the 1D model (Figure 8b). This scatter is likely caused by the 3D velocity field in the immediate vicinity of the hypocenters (i.e., within a single cell), which can be seen as the source-side analog to the station corrections in the minimum 1D approach. For less constrained hypocenters (e.g., larger gap, few observations, and presence of erroneous phase interpretations) the 3D velocity grid might actually enhance distortions and bias of the solution rather than absorb it. In our proposed strategy, this scatter can be minimized by a subsequent relative relocation, resulting in the most accurate and precise set of hypocenters, with accuracies comparable to very local velocity models (Figure 8c).

The 1σ location error estimated by the NLL algorithm with the *L*2-misfit function appears realistic for well-constrained *Pg*-*Sg* solutions and includes the true location in synthetic and most GT tests (Figures 3 and 8). However, its reliability is strongly coupled to the accuracy of the velocity model and might be significantly overestimated (i.e., too optimistic) in case of improper velocity models (regional minimum 1D model in Figure 8a, quarry blast locations in Figure 8f, or usage of phases ≥80 km in Figure 3). The *L*2-based error might also be unrealistically small and not representative of the true location accuracy in cases of poorly constrained solutions, because the assumed Gaussian estimators might underestimate the non-linearity of the corresponding probability density functions, resulting in an underestimation of the true location uncertainties (e.g., Husen et al., 2003). We also assessed the error derived with an alternative misfit function, which is implemented as the equal-differential-time (EDT) method in NLL (e.g., Font et al., 2004; Lomax et al., 2014). The resulting 1σ errors were unrealistically large (i.e., too pessimistic) for well-constrained locations in our dataset. We therefore prefer the *L*2-misfit function and combine the NLL error with additional network criteria to ensure that only robust locations and uncertainties are considered for interpretation in Figures 10 and 11.

Constraining the focal depth with the proposed *Pg*-*Sg* relocation procedure requires a dense network to obtain depth-constraining *Pg* and *Sg* phases within epicentral distances of about 1.5 times the focal depth (see Section 2.1). To ensure that true focal depths ≥6 km are constrained uniformly across a seismic network therefore requires an average station spacing of about 20 km. Figure S13a shows interpolated interstation distances for the study region (network geometry as of December 31, 2020) following the approach of Kuyuk and Allen (2013). The median interstation distance for stations operated by the SED and collaborating networks in the Central Alps region is 10 km and therefore in the range of values reported by Kuyuk and Allen (2013) for California (15 km) or Japan (19 km). The station spacing in most parts of Switzerland is ≤20 km and in some densely instrumented regions ≤10 km. Figure S13b documents that the distance to the closest station is ≤10 km in most parts of Switzerland and ≤5 km in densely instrumented regions. In agreement with minimum distances achieved for relocations in the period of 2010–2020 (Figure 9), we conclude that focal depths of the majority of upper-crustal seismicity (true focal depth ≥3–6 km) is well constrained by *Pg* and *Sg* phases with the current network geometry. As demonstrated by quarry blasts locations in Figure 8f, even focal depths of near-surface sources may be reliably resolved with this procedure. Procedures relying on additional, *a priori* earth structure from other geophysical methods (e.g., geometry of sedimentary basins or Moho), combined with regional *Pg*, *Pn*, and *PmP* phases as proposed for example, by Wagner et al. (2013) or Theunissen et al. (2017) may in principle improve focal-depth estimates in the case of sparser networks. However, since the accuracy of the derived focal depths depends directly on the model uncertainties (±few kilometers for the Moho, e.g., Waldhauser et al., 1998), the sub-kilometer accuracy targeted in this study is typically not achievable with these procedures.

5.3. Relocated Seismicity and Joint Interpretation With Velocity Structure in the Central Alps Region

The new velocity models and the consistently relocated seismicity derived in this study form the basis for future high-resolution seismotectonic interpretations of the Central Alps and their foreland. In the following sections, we will restrict the discussion to selected seismogenic structures, documenting the improvements achieved in this study. As demonstrated by Figures 10b and 10c, the improvement in accuracy and precision of the relocated seismicity is best visible for earthquake clusters at scales of a few kilometers. However, the relocated catalog also reveals some new seismogenic structures, which have been previously unrecognized. One prominent example is an NNE-SSW striking earthquake lineament labeled “Schwarzwasser Lineament” in Figure 10a, which locates in

the Swiss Molasse basin and ranges from the city of Bern to the Alpine front. This lineament runs parallel to and east of the neighboring Fribourg Fault (FF in Figure 10a), which is a vertical strike-slip fault presumably located within the sedimentary cover of the Molasse basin (e.g., Kastrup et al., 2007; Vouillamoz et al., 2017). This newly imaged Schwarzwasser Lineament therefore indicates the presence of another seismically active NS-striking, shallow, sub-parallel strike-slip fault system in the western part of the Swiss Molasse basin. Another prominent earthquake lineament visible in the northern Alpine foreland is a NW-SE striking cluster extending from the city of Basel to Läufelfingen in the Jura Mountains ("Basel-Läufelfingen Lineament" in Figure 10a). Focal depths associated with this lineament range from 5 to 20 km, indicating a potential crustal-scale zone of localized deformation beneath the eastern Jura Mountains southeast of Basel.

Within the Alps, several earthquake lineaments north and south of the RSL can be observed in southwest Switzerland. In addition to the two main bands of seismicity identified and discussed in earlier studies (e.g., Maurer et al., 1997), the relocated seismicity reveals several new branches (Figure 10a). These branches indicate a continuation of fault zones toward the southwest and therefore suggest a possible link to fault systems in the Western Alps. Relocations in the eastern part of the study region suggests a more diffuse distribution of seismicity. Clusters of increased seismic activity locate in the Penninic and Austroalpine realms to both sides of the Engadine fault as well as in the Helvetic realm adjacent to the Alpine front (Figure 10a).

In 2017, the M_L 4.6 Urnerboden earthquake (Figure 10a), one of the largest instrumentally recorded earthquakes in the Central Alps, occurred in the aforementioned Helvetic realm. From the analysis of focal mechanisms and relative relocations of fore- and aftershocks, Diehl et al. (2021) concluded that the earthquake is associated with an NNW-SSE striking sinistral strike-slip fault (see Figure 10a). We use this earthquake as an example to demonstrate how the derived 3D V_P and V_S structures and relocated hypocenters can be jointly interpreted to constrain the lithology hosting upper-crustal seismicity. Figure 11 shows vertical cross-sections of well-constrained relocated hypocenters in combination with V_P, V_S, and V_P/V_S ratios of the M_L 4.6 source region and the frontal part of the Central Alps. Figures 11c includes a geological interpretation based on geological profiles of Oberholzer (1933), the interpolated top-basement model of Pfiffner (2014) and results of a recent 3D structural model of the Aar massif. Seismic velocities of $V_P > 5.8$ km/s and $V_S > 3.5$ km/s in the source region of the M_L 4.6 earthquake (Figures 11a and 11b) are indicative for granitic-gneissic rocks (e.g., Christensen, 1996) and point to a source in the crystalline basement of the northern Aar Massif, consistent with the geological model (Figures 11c). This interpretation is further supported by the relatively low V_P/V_S ratio of about 1.625–1.675 computed from the independent V_P and V_S models in the source region (Figures 11c). Such low V_P/V_S ratio falls at the lowermost bound expected for granitic-gneissic rocks (e.g., Christensen, 1996) and is certainly incompatible with a source located in the sedimentary cover of the Aar Massif. The lower than average V_P/V_S ratio imaged for the Aar Massif by our tomographic inversion is in good agreement with low V_P/V_S ratios of about 1.68 derived from receiver functions in the Helvetic domain (Lombardi et al., 2008) and suggests a felsic composition of the uplifted crustal block, possibly with increased quartz content. In contrast, Subalpine Molasse and Flysch units as well as limestone dominated Helvetic nappes in the frontal part of the Alps are characterized by a high V_P/V_S ratio (Figures 11c), indicative for lithologies dominated by sedimentary rocks. In conclusion, our results regarding the Urnerboden earthquake suggest active strike-slip deformation within the eastern Aar massif, which is possibly related to along-strike differences in the present-day uplift processes of this external massif as suggested by Nibourel et al. (2021).

6. Conclusion

This study demonstrates on the basis of synthetic tests and selected GT events that a sub-kilometer hypocenter accuracy can be achieved by combining accurate, regional-scale 3D upper-crustal *P* and *S* wave velocity models with dynamically selected *Pg* and *Sg* phases of a dense seismic network. We propose a strategy to achieve accurate crustal velocity models using well-established LET methods and a thorough, multi-stage quality control of *Pg* and *Sg* arrival-time data. Different tomographic inversion strategies have been tested in order to assess the compatibility of the derived V_P and V_S models. From these tests we conclude that independent inversions of high-quality *P* and *S* phase data converge to the same solutions as solutions derived from joint inversions. The benefit of the proposed independent inversion is that it allows for a reliable quality control of phase data as well as the unbiased assessment of LET inversion parameters, model resolution, and petrophysical properties. This strategy therefore provides unbiased, self-consistent solutions of the 3D V_P and V_S field. Differences between *P*- and

S-based hypocenters as well as travel-time residuals need to be assessed, however, to ensure that the independent models result in consistent hypocenter locations when combined in the relocation procedure. Joint inversion of *P* and *S* phases is potentially the preferred strategy in case quality and quantity of *S* data do not allow for an independent inversion. However, the derived models could be biased, for example, by the imbalance between *P* and *S* data, undetected inconsistencies in the arrival times or improper inversion parameters.

The procedure is applied to the Central Alps region, with its weak to moderate seismic activity. The exceptional density of the seismic network provides epicenter-near *Pg* and *Sg* observations to accurately constrain shallow focal depths ≥3–6 km in most parts of the region. The derived 3D models image the V_P and V_S structure of the upper crust of the Central Alps and their foreland with unprecedented resolution, revealing small-scale features such as those related to Subalpine Molasse sediments residing below the Helvetic nappes near the Alpine front. The new V_P and V_S models are used to relocate the instrumental earthquake bulletin of the SED for the period 1984/01 to 2020/05. We demonstrate that the proposed relocation procedure can achieve sub-kilometer hypocenter accuracy and formal 1σ uncertainty estimates are realistic for the majority of well-constrained hypocenters.

The relocated seismicity documents improvements for earthquake clusters at scales of few kilometers and also identifies several new seismogenic structures like the "Schwarzwasser Lineament" located in the Swiss Molasse basin south of Bern. The M_L 4.6 Urnerboden earthquake of 2017 is used as an example to demonstrate how the derived 3D velocity structure and relocated hypocenters can be jointly interpreted to constrain the lithology hosting upper-crustal seismicity in the study region. Values of V_P, V_S, and V_P/V_S ratio in the source region of the M_L 4.6 earthquake point to a source in the crystalline basement of the northern Aar Massif. We relate the lower than average V_P/V_S ratio of about 1.625–1.675 found for the Aar Massif to a felsic composition of the uplifted crustal block, possibly with increased quartz content. In conclusion, the newly derived velocity models and the consistently relocated seismicity derived in this study form the basis for future high-resolution seismotectonic studies in the Central Alps and their foreland. In addition, the improved absolute hypocenter locations will be used as initial locations for future relative-relocation studies, which will provide new insights into the relation between seismicity and geologically and geophysically mapped faults.

Data Availability Statement

Additional data recorded by temporary networks in Switzerland have been used in this study (network codes 8D, 4D, XP, XY; Swiss Seismological Service (SED) at ETH Zurich, 1985, 2005, 2012, and 2018). Waveform data from the SED permanent seismic network (network code CH) as well as the majority of waveform data collected by collaborating networks (network codes listed above) in the greater Alpine region are openly available through the European Integrated Data Archive (EIDA): http://www.orfeus-eu.org/data/eida/. Waveform data collected by temporary networks in Switzerland in the framework of PhD studies or in collaboration with industry might be restricted or embargoed. Phase data used for tomographic inversion as well as derived velocity models (1D and 3D) and catalogs with relocated earthquakes and blasts presented in this study are provided in a permanent data repository (https://doi.org/10.3929/ethz-b-000453236).

Acknowledgments
Comments by the associate editor, four anonymous reviewers, and Anthony Lomax helped to improve the manuscript and are thankfully acknowledged. The authors gratefully acknowledge inspiring discussions with Nicolas Deichmann and Stephan Husen in advance of this study. Furthermore, they thank Ferdinando Musso for helpful discussions and providing 3D structural data of the Aar Massif. Financial support from the Nationale Genossenschaft für die Lagerung radioaktiver Abfälle (Nagra) for the research presented in this study is gratefully acknowledged. The authors are grateful for support by the Swiss Geophysical Commission in the framework of the SeismoTeCH project. They acknowledge the cooperation with the AlpArray Working Group (www.alparray.ethz.ch) and the operation of the AlpArray temporary seismic network Z3 (AlpArray Seismic Network, 2015; see also Hetényi et al., 2018). AlpArray Switzerland is funded by the Swiss-AlpArray SINERGIA project CRSII2_154434/1 by the Swiss National Science Foundation (SNSF). The authors acknowledge the collaboration with permanent seismic networks used in this study: BW (Department of Earth and Environmental Sciences, Geophysical observatory, University of Munich, 2001), C4 (CERN, 2016), CH (Swiss Seismological Service (SED) At ETH Zurich, 1983), FR (RESIF, 1995), GR (Federal Institute for Geosciences and Natural Resources, 1976), GU (University of Genova, 1967), IV (INGV Seismological Data Centre, 2006), LE (Landeserdbebendienst Baden-Wuerttemberg, Regierungspraesidium Freiburg, 2009), MN (MedNet Project Partner Institutions, 1990), NI (OGS (Istituto Nazionale di Oceanografia e di Geofisica Sperimentale) and University of Trieste, 2002), OE (ZAMG - Zentralanstalt für Meterologie und Geodynamik, 1987), OX (Istituto Nazionale di Oceanografia e di Geofisica Sperimentale - OGS, 2016), RA (RESIF, 1995), SI (Provincia autonoma di Bolzano, Province Südtirol network). Open access funding provided by Eidgenossische Technische Hochschule Zurich.

References

AlpArray Seismic Network. (2015). *AlpArray seismic network (AASN) temporary component*. AlpArray Working Group. https://doi.org/10.12686/alparray/z3_2015

Bondár, I., Myers, S., Engdahl, E., & Bergman, E. (2004). Epicentre accuracy based on seismic network criteria. *Geophysical Journal International*, *156*(3), 483–496. https://doi.org/10.1111/j.1365-246X.2004.02070.x

CERN. (2016). *CERN Seismic Network*. ETH Zurich. https://doi.org/10.12686/sed/networks/c4

Chatelain, J. L., Roecker, S. W., Hatzfeld, D., & Molnar, P. (1980). Microearthquake seismicity and fault plane solutions in the Hindu Kush Region and their tectonic implications. *Journal of Geophysical Research*, *85*(B3), 1365–1387. https://doi.org/10.1029/JB085iB03p01365

Christensen, N. I. (1996). Poisson's ratio and crustal seismology. *Journal of Geophysical Research*, *101*(B2), 3139–3156. https://doi.org/10.1029/95jb03446

Deichmann, N. (1992). Structural and rheological implications of lower-crustal earthquakes below Northern Switzerland. *Physics of the Earth and Planetary Interiors*, *69*(3–4), 270–280. https://doi.org/10.1016/0031-9201(92)90146-m

Deichmann, N., Baer, M., Braunmiller, J., & Dolfin, D. B. (2000). Earthquakes in Switzerland and surrounding regions during 1999. *Eclogae Geologicae Helvetiae*, *93*(3), 395–406.

Department of Earth and Environmental Sciences, Geophysical observatory, University of Munich. (2001). BayernNetz [Data set]. International Federation of Digital Seismograph Networks. https://doi.org/10.7914/SN/BW

Diehl, T., Clinton, J., Cauzzi, C., Kraft, T., Kästli, P., Deichmann, N., et al. (2021). Earthquakes in Switzerland and surrounding regions during 2017 and 2018. *Swiss Journal of Geosciences*, *114*(4). https://doi.org/10.1186/s00015-020-00382-2

Diehl, T., Clinton, J., Deichmann, N., Cauzzi, C., Kästli, P., Kraft, T., et al. (2018). Earthquakes in Switzerland and surrounding regions during 2015 and 2016. *Swiss Journal of Geosciences*, *111*(1), 221–244. https://doi.org/10.1007/s00015-017-0295-y

Diehl, T., Deichmann, N., Husen, S., & Kissling, E. (2005). Assessment of quality and consistency of S-wave arrivals in local earthquake data. *Geophysical Research Abstracts*, *7*, 04912.

Diehl, T., Husen, S., Kissling, E., & Deichmann, N. (2009). High-resolution 3-D P-wave model of the Alpine crust. *Geophysical Journal International*, *179*(2), 1133–1147. https://doi.org/10.1111/J.1365-246x.2009.04331.X

Diehl, T., Kissling, E., & Bormann, P. (2012). Chapter: IS 11.4: Tutorial for consistent phase picking at local to regional distances. In P. Bormann (Ed.), *New manual of seismological observatory practice 2 (NMSOP-2)* (pp. 1–21). Potsdam: German Research Centre for Geosciences. https://doi.org/10.2312/GFZ.NMSOP-2_IS_11.4

Diehl, T., Kissling, E., Husen, S., & Aldersons, F. (2009). Consistent phase picking for regional tomography models: Application to the greater Alpine region. *Geophysical Journal International*, *176*, 542–554. https://doi.org/10.1111/j.1365-246X.2008.03985.x

Diehl, T., Kraft, T., Kissling, E., & Wiemer, S. (2017). The induced earthquake sequence related to the St. Gallen deep geothermal project (Switzerland): Fault reactivation and fluid interactions imaged by microseismicity. *Journal of Geophysical Research: Solid Earth*, *122*(9), 7272–7290. https://doi.org/10.1002/2017JB014473

Eberhart-Phillips, D. (1990). Three-dimensional P and S velocity structure in the Coalinga region, California. *Journal of Geophysical Research*, *95*, 15343–15363. https://doi.org/10.1029/jb095ib10p15343

Eberhart-Phillips, D., & Reyners, M. (2012). Imaging the Hikurangi Plate interface region, with improved local-earthquake tomography. *Geophysical Journal International*, *190*(2), 1221–1242. https://doi.org/10.1111/j.1365-246X.2012.05553.x

Ellsworth, W. L. (2013). Injection-induced earthquakes. *Science*, *341*(6142), 1225942–1225942. https://doi.org/10.1126/science.1225942

Engdahl, E. R., van der Hilst, R., & Buland, R. (1998). Global teleseismic earthquake relocation with improved travel times and procedures for depth determination. *Bulletin of the Seismological Society of America*, *88*(3), 722–743.

Federal Institute for Geosciences and Natural Resources. (1976). *German Regional Seismic Network (GRSN)*. Bundesanstalt für Geowissenschaften und Rohstoffe. https://doi.org/10.25928/MBX6-HR74

Font, Y., Kao, H., Lallemand, S., Liu, C.-S., & Chiao, L.-Y. (2004). Hypocentre determination offshore of eastern Taiwan using the maximum intersection method. *Geophysical Journal International*, *158*(2), 655–675. https://doi.org/10.1111/j.1365-246X.2004.02317.x

Gaucher, E., Schoenball, M., Heidbach, O., Zang, A., Fokker, P. A., van Wees, J.-D., & Kohl, T. (2015). Induced seismicity in geothermal reservoirs: A review of forecasting approaches. *Renewable & Sustainable Energy Reviews*, *52*, 1473–1490. https://doi.org/10.1016/j.rser.2015.08.026

Goertz-Allmann, B. P., Gibbons, S. J., Oye, V., Bauer, R., & Will, R. (2017). Characterization of induced seismicity patterns derived from internal structure in event clusters. *Journal of Geophysical Research: Solid Earth*, *122*(5), 3875–3894. https://doi.org/10.1002/2016JB013731

Gomberg, J. S., Shedlock, K. M., & Roecker, S. W. (1990). The effect of S-wave arrival times on the accuracy of the hypocenter estimation. *Bulletin of the Seismological Society of America*, *80*, 1605–1628. https://doi.org/10.1785/bssa08006a1605

Haslinger, F., & Kissling, E. (2001). Investigating effects of 3-D ray tracing methods in local earthquake tomography. *Physics of the Earth and Planetary Interiors*, *123*(2–4), 103–114. https://doi.org/10.1016/S0031-9201(00)00204-1

Hetényi, G., Molinari, I., Clinton, J., Bokelmann, G., Bondár, I., Crawford, W. C., et al. (2018). The AlpArray seismic network: A large-scale European experiment to image the Alpine Orogen. *Surveys in Geophysics*, *39*(5), 1009–1033. https://doi.org/10.1007/s10712-018-9472-4

Heuberger, S., Roth, P., Zingg, O., Naef, H., & Meier, B. P. (2016). The St. Gallen Fault Zone: A long-lived, multiphase structure in the North Alpine Foreland Basin revealed by 3D seismic data. *Swiss Journal of Geosciences*, *109*(1), 83–102. https://doi.org/10.1007/s00015-016-0208-5

Husen, S., & Hardebeck, J. L. (2010). *Earthquake location accuracy*. Community Online Resource for Statistical Seismicity Analysis. https://doi.org/10.5078/corssa-55815573

Husen, S., Kissling, E., & Clinton, J. F. (2011). Local and regional minimum 1D models for earthquake location and data quality assessment in complex tectonic regions: Application to Switzerland. *Swiss Journal of Geosciences*, *104*(3), 455–469. https://doi.org/10.1007/s00015-011-0071-3

Husen, S., Kissling, E., Deichmann, N., Wiemer, S., Giardini, D., & Baer, M. (2003). Probabelistic earthquake location in complex three-dimensional velocity models: Application to Switzerland. *Journal of Geophysical Research*, *108*, 2077. https://doi.org/10.1029/2002JB001778

Husen, S., Kissling, E., Flueh, E. R., & Asch, G. (1999). Accurate hypocentre determination in the seismogenic zone of the subducting Nazca plate in northern Chile using a combined on-/offshore network. *Geophysical Journal International*, *105*, 687–701. https://doi.org/10.1046/j.1365-246x.1999.00893.x

INGV Seismological Data Centre. (2006). *Rete Sismica Nazionale (RSN)*. Italy: Istituto Nazionale di Geofisica e Vulcanologia (INGV). https://doi.org/10.13127/SD/X0FXnH7QfY

Istituto Nazionale di Oceanografia e di Geofisica Sperimentale - OGS. (2016). North-East Italy Seismic Network [Data set]. FDSN. https://doi.org/10.7914/SN/OX

Kastrup, U., Deichmann, N., Fröhlich, A., & Giardini, D. (2007). Evidence for an active fault below the northwestern Alpine foreland of Switzerland. *Geophysical Journal International*, *169*(3), 1273–1288. https://doi.org/10.1111/J.1365-246x.2007.03413.X

Kim, W.-Y., Dineva, S., Ma, S., & Eaton, D. (2006). The 4 August 2004, Lake Ontario, earthquake. *Seismological Research Letters*, *77*(1), 65–73. https://doi.org/10.1785/gssrl.77.1.65

Kissling, E. (1988). Geotomography with local earthquake data. *Review of Geophysics*, *26*, 659–698. https://doi.org/10.1029/rg026i004p00659

Kissling, E., Ellsworth, W. L., Phillips, E. D., & Kradolfer, U. (1994). Initial reference models in local earthquake tomography. *Journal of Geophysical Research*, *99*(B10), 19635–19646. https://doi.org/10.1029/93JB03138

Kissling, E., Husen, S., & Haslinger, F. (2001). Model parametrization in seismic tomography: A choice of consequence for the solution quality. *Physics of the Earth and Planetary Interiors*, *123*, 89–101. https://doi.org/10.1016/s0031-9201(00)00203-x

Kisslinger, C., & Engdahl, E. R. (1973). The interpretation of the Wadati diagram with relaxed assumptions. *Bulletin of the Seismological Society of America*, *63*, 1723–1736.

Kuyuk, H. S., & Allen, R. M. (2013). Optimal seismic network density for earthquake early warning: A case study from California. *Seismological Research Letters*, *84*(6), 946–954. https://doi.org/10.1785/0220130043

Landeserdbebendienst Baden-Wuerttemberg, Regierungspraesidium Freiburg. (2009). Landeserdbebendienst Baden-Wuerttemberg [Data set]. International Federation of Digital Seismograph Networks. https://doi.org/10.7914/SN/LE

Lin, G., Shearer, P. M., Hauksson, E., & Thurber, C. H. (2007). A three-dimensional crustal seismic velocity model for southern California from a composite event method. *Journal of Geophysical Research: Solid Earth*, *112*(B11), B11306. https://doi.org/10.1029/2007JB004977

Lomax, A., Michelini, A., & Curtis, A. (2014). Earthquake location, direct, global-search methods. In R. Meyers (Ed.) *Encyclopedia of complexity and systems science* (pp. 1–33). New York, NY: Springer. https://doi.org/10.1007/978-3-642-27737-5_150-2

Lomax, A., Virieux, J., Volant, P., & Berge-Thierry, C. (2000). Probabilistic earthquake location in 3D and layered models. In C. H. Thurber & N. Rabinowitz (Eds.), *Advances in seismic event location* (pp. 101–134). London: Kluwer Academic Publishers, https://doi.org/10.1007/978-94-015-9536-0_5

Lombardi, D., Braunmiller, J., Kissling, E., & Giardini, D. (2008). Moho depth and Poisson's ratio in the western-central Alps from receiver functions. *Geophysical Journal International*, *173*, 249–264. https://doi.org/10.1111/j.1365-246X.2007.03706.x

Luetgert, J. H. (1992). *MacRay: Interactive two-dimensional seismic raytracing for the Macintosh* (No. 92–356, pp. 1–2). US Geological Survey Open-File Report.

Ma, S. (2010). Focal depth determination for moderate and small earthquakes by modeling regional depth phases sPg, sPmP, and sPn. *Bulletin of the Seismological Society of America*, *100*(3), 1073–1088. https://doi.org/10.1785/0120090103

Maurer, H., & Kradolfer, U. (1996). Hypocentral parameters and velocity estimation in the western Swiss Alps by simultaneous inversion of P- and S-wave data. *Bulletin of the Seismological Society of America*, *86*, 32–42.

Maurer, H. R., Burkhard, M., Deichmann, N., & Green, A. G. (1997). Active tectonism in the central Alps: Contrasting stress regimes north and south of the Rhone Valley. *Terra Nova*, *9*(2), 91–94. https://doi.org/10.1111/j.1365-3121.1997.tb00010.x

Michelini, A., & McEvilly, T. V. (1991). Seismological studies at Parkfield, I, Simultaneous inversion for velocity structure and hypocenters using cubic B-splines parameterization. *Bulletin of the Seismological Society of America*, *81*, 524–552.

MedNet Project Partner Institutions. (1990). *Mediterranean very broadband seismographic network (MedNet)*. Italy: Istituto Nazionale di Geofisica e Vulcanologia (INGV). https://doi.org/10.13127/SD/fBBBtDtd6q

Mock, S., & Herwegh, M. (2017). Tectonics of the central Swiss Molasse Basin: Post-Miocene transition to incipient thick-skinned tectonics? *Tectonics*, *36*(9), 1699–1723. https://doi.org/10.1002/2017TC004584

Mosar, J. (1999). Present-day and future tectonic underplating in the western Swiss Alps: Reconciliation of basement/wrench-faulting and décollement folding of the Jura and Molasse basin in the Alpine foreland. *Earth and Planetary Science Letters*, *173*(3), 143–155. https://doi.org/10.1016/S0012-821X(99)00238-1

Moser, T. J., van Eck, T., & Nolet, G. (1992). Hypocenter determination in strongly heterogeneous earth models using the shortest path method. *Journal of Geophysical Research*, *97*, 6563–6572. https://doi.org/10.1029/91jb03176

Nibourel, L., Rahn, M., Dunkl, I., Berger, A., Herman, F., Diehl, T., et al. (2021). Orogen-parallel migration of exhumation in the eastern Aar Massif revealed by low-T thermochronometry. *Journal of Geophysical Research: Solid Earth*, *126*, e2020JB020799. https://doi.org/10.1029/2020JB020799

Oberholzer, J. (1933). *Geologie der Glarneralpen. – Beiträge zur Geologischen Karte der Schweiz*. Schweiz. Geol. Komm. Liefg. Nr. 28.

OGS (Istituto Nazionale di Oceanografia e di Geofisica Sperimentale) and University of Trieste. (2002). North-East Italy Broadband Network. International Federation of Digital Seismograph Networks [Data set]. https://doi.org/10.7914/SN/NI

Pavlis, G. L. (1986). Appraising earthquake hypocenter location errors - A complete, practical approach for single-event locations. *Bulletin of the Seismological Society of America*, *76*, 1699–1717.

Pfiffner, O. A. (2014). *Geology of the Alps*. Wiley.

Pfiffner, O. A. (2017). Thick-skinned and thin-skinned tectonics: A global perspective. *Geosciences*, *7*(3), 71. https://doi.org/10.3390/geosciences7030071

Podvin, P., & Lecomte, I. (1991). Finite difference computation of travel times in very contrasted velocity models: A massively parallel approach and its associated tools. *Geophysical Journal International*, *105*, 271–284. https://doi.org/10.1111/j.1365-246x.1991.tb03461.x

RESIF. (1995). RESIF-RLBP French Broad-band network, RESIF-RAP strong motion network and other seismic stations in metropolitan France [Data set]. RESIF - Réseau Sismologique et géodésique Français. https://doi.org/10.15778/RESIF.FR

Reyners, M., Eberhart-Phillips, D., & Stuart, G. (1999). A three-dimensional image of the shallow subduction: Crustal structure of the Raukumara Peninsula. New Zealand, *Geophysical Journal International*, *137*, 873–890. https://doi.org/10.1046/j.1365-246x.1999.00842.x

Singer, J., Diehl, T., Husen, S., Kissling, E., & Duretz, T. (2014). Alpine lithosphere slab rollback causing lower crustal seismicity in northern foreland. *Earth and Planetary Science Letters*, *397*, 42–56. https://doi.org/10.1016/J.Epsl.2014.04.002

Stroujkova, A. (2009). Constraining event depths and crustal velocities using regional depth phases. *Bulletin of the Seismological Society of America*, *99*(1), 215–225. https://doi.org/10.1785/0120080085

Swiss Seismological Service (SED) At ETH Zurich. (1983). *National Seismic Networks of Switzerland*. ETH Zürich. https://doi.org/10.12686/sed/networks/ch

Swiss Seismological Service (SED) at ETH Zurich. (1985). *Temporary deployments in Switzerland associated with glacier monitoring*. ETH Zurich. https://doi.org/10.12686/sed/networks/4d

Swiss Seismological Service (SED) at ETH Zurich. (2005). *Temporary deployments in Switzerland associated with aftershocks and other seismic sequences*. ETH Zurich. https://doi.org/10.12686/sed/networks/8d

Swiss Seismological Service (SED) at ETH Zurich. (2012). *Temporary deployments in Switzerland associated with landslides*. ETH Zurich. https://doi.org/10.12686/sed/networks/xp

Swiss Seismological Service at ETH Zurich. (2018). *Stations deployed for risk model Switzerland*. ETH Zurich. https://doi.org/10.12686/sed/networks/xy

Swisstopo. (2005). *Tectonic map of Switzerland 1:500,000*. Wabern: Federal Office of Topography Swisstopo.

Tarantola, A., & Valette, B. (1982). Inverse problems = Quest for information. *Journal of Geophysics*, *50*(1), 159–170.

Theunissen, T., Chevrot, S., Sylvander, M., Monteiller, V., Calvet, M., Villasenor, A., et al. (2017). Absolute earthquake locations using 3-D versus 1-D velocity models below a local seismic network: Example from the Pyrenees. *Geophysical Journal International*, *212*(3), 1806–1828. https://doi.org/10.1093/gji/ggx472

Thurber, C. H. (1983). Earthquake locations and three-dimensional crustal structure in the Coyote Lake area, central California. *Journal of Geophysical Research*, *88*, 8226–8236. https://doi.org/10.1029/jb088ib10p08226

Thurber, C. H. (1993). Local earthquake tomography: Velocities and V_P/V_S-theory. In H. M. Iyer & K. Hirahara (Eds.), *Seismic tomography* (pp. 563–583). London:Chapman & Hall.

Tryggvason, A., Rögnvaldsson, S. T., & Flóvenz, Ó. G. (2002). Three-dimensional imaging of the P- and S-wave velocity structure and earthquake locations beneath Southwest Iceland. *Geophysical Journal International*, *151*(3), 848–866. https://doi.org/10.1046/j.1365-246X.2002.01812.x

University of Genova. (1967). Regional Seismic Network of North Western Italy [Data set]. International Federation of Digital Seismograph Networks. https://doi.org/10.7914/SN/GU

Ustaszewski, K., & Schmid, S. M. (2007). Latest Pliocene to recent thick-skinned tectonics at the Upper Rhine Graben – Jura Mountains junction. *Swiss Journal of Geosciences*, *100*(2), 293–312. https://doi.org/10.1007/s00015-007-1226-0

Vouillamoz, N., Mosar, J., & Deichmann, N. (2017). Multi-scale imaging of a slow active fault zone: Contribution for improved seismic hazard assessment in the Swiss Alpine foreland. *Swiss Journal of Geosciences*, *110*(2), 547–563. https://doi.org/10.1007/s00015-017-0269-0

Wagner, M., Husen, S., Lomax, A., Kissling, E., & Giardini, D. (2013). High-precision earthquake locations in Switzerland using regional secondary arrivals in a 3-D velocity model. *Geophysical Journal International*, *193*(3), 1589–1607. https://doi.org/10.1093/gji/ggt052

Waldhauser, F., & Ellsworth, W. L. (2000). A double-difference earthquake location algorithm: Method and application to the northern Hayward fault, California. *Bulletin of the Seismological Society of America*, *90*(6), 1353–1368. https://doi.org/10.1785/0120000006

Waldhauser, F., Kissling, E., Ansorge, J., & Mueller, S. (1998). Three-dimensional interface modelling with two-dimensional seismic data: The Alpine crust-mantle boundary. *Geophysical Journal International*, *135*(1), 264–278. https://doi.org/10.1046/j.1365-246X.1998.00647.x

Zandt, G., & Ammon, C. J. (1995). Continental crust composition constrained by measurements of crustal Poisson's ratio. *Nature*, *374*, 152–154. https://doi.org/10.1038/374152a0

ZAMG - Zentralanstalt für Meterologie und Geodynamik. (1987). Austrian seismic network [Data set]. International Federation of Digital Seismograph Networks. https://doi.org/10.7914/SN/OE